Revised, November.**01**.2016, ACS Applied Materials & Interfaces,
a) The final revised manuscript file that does not contain any highlighting or editing marks. This file should be uploaded as the primary manuscript document file.

Hybridization of zinc oxide tetrapods for selective gas sensing applications

O. Lupan,[1,] V. Postica,[2] J. Gröttrup,[1] A. K. Mishra,[3] Nora H. de Leeuw,[3,4,*] J. F. C. Carreira,[5] J. Rodrigues,[5] N. Ben Sedrine,[5] Maria R. Correia,[5,*] Teresa Monteiro,[5] V. Cretu,[2] I. Tiginyanu,[2] Daria Smazna,[1] Y. K. Mishra,[1] R. Adelung[1,*]*

[1] *Functional Nanomaterials, Institute for Materials Science, Christian-Albrechts Universität zu Kiel, Kiel University, Kaiserstr. 2, D-24143, Kiel, Germany*
[2] *Department of Microelectronics and Biomedical Engineering, Technical University of Moldova, 168 Stefan cel Mare Av., MD-2004 Chisinau, Republic of Moldova*
[3] *Department of Chemistry, University College London, 20 Gordon Street, London WC1H 0AJ, U.K.* [3] *Research & Develoment, University of Petroleum and Energy Studies (UPES), Bidholi, Dehradun 248007, India*
[4] *School of Chemistry, Cardiff University, Main Building, Park Place, Cardiff CF10 3AT, U.K.*
[5] *Department of Physics and I3N, Institute for Nanostructures, Nanomodelling and Nanofabrication, University of Aveiro, 3810-193 Aveiro, Portugal*

*Corresponding authors
Prof. Dr.Eng. O. Lupan (ollu@tf.uni-kiel.de)
Prof. Nora H. de Leeuw
Prof. Maria Rosário Correia
Prof. R. Adelung

ABSTRACT

In this work, the exceptionally improved sensing capability of highly porous 3-D hybrid ceramic networks with respect to reducing gases is demonstrated for the first time. The 3-D hybrid ceramic networks are based on metal oxides (Me_xO_y and $Zn_xMe_{1-x}O_y$, Me= Fe, Cu, Al) doped and alloyed zinc oxide tetrapods (ZnO-T) forming numerous heterojunctions. A change in morphology of the samples and formation of different complex microstructures is achieved by mixing the metallic (Fe, Cu, Al) microparticles with ZnO tetrapods grown by flame transport synthesis (FTS) approach with different weight ratios (ZnO:Me, e.g., 20:1) and followed by subsequent thermal annealing them in air. The gas sensing studies reveal the possibility to control and change/tune the selectivity of the materials, depending on the elemental content ratio and the type of the added metal oxide in 3-D ZnO-T hybrid networks. While pristine ZnO-T networks showed a good response to H_2 gas, a change/tune in selectivity to ethanol vapour with a decrease in optimal operating temperature was observed in the networks hybridized with Fe-oxide and Cu-oxide. In case of hybridization with $ZnAl_2O_4$ an improvement of H_2 gas response (to $\approx$ 7.5) was reached at lower doping concentrations (20:1), whereas the increasing in concentration of $ZnAl_2O_4$ (10:1), the selectivity changes to methane CH_4 gas (response $\approx$ 28). Selectivity tuning to different gases is attributed to the catalytic properties of the metal oxides after hybridization, while the sensitivity improvement is mainly associated with additional modulation of resistance by the built-in potential barriers between *n-n* and *n-p* heterojunctions, during adsorption and desorption of gaseous species. Density functional theory based calculations provided the mechanistic insights into the interactions between different hybrid networks and gas molecules supporting the experimentally observed results. The studied materials and sensor structures would provide particular advantages in the field of fundamental research, industrial and ecological applications.

KEYWORDS: Hybrid, ZnO tetrapod, selectivity, gas sensor, hydrogen sensor, DFT study.

1. INTRODUCTION

Hybrid nanostructured networks from semiconducting oxides have demonstrated exceptional sensing properties with fast and highly sensitive detection of inflammable and toxic gases.[1-3] Nanoarchitectures of semiconducting oxides are becoming important advanced materials with a large variety of exceptional properties for an extensive utilization, ranging from ultraviolet (UV) and gas sensing to biomedical and catalyst applications.[2-3] However, the rapid progress in nanotechnologies includes the continuous search of novel materials with new and unique functionalities, which is in focus of many research groups around the world.[1-6] In this context, fabrication of three-dimensional (3-D) networks of interconnected ZnO tetrapods (ZnO-T) has been a very important step for progress in engineering, science and nanotechnology.[1, 3-4, 6-8] Recently the research group of Rainer Adelung has demonstrated a fast and simple synthesis of highly porous interconnected ZnO-T networks by a crucible flame transport synthesis (C-FTS) approach and burner flame transport synthesis (B-FTS).[1, 3-4] The B-FTS approach can be characterized by a rapid synthesis process in only 3–5 s of highly crystalline interconnected ZnO nanotetrapod-network.[1] Such metal oxide networks have shown excellent multifunctional and further attractive properties, including fast and sensitive UV detection, as well as significant photocatalytic activity.[1, 3] Due to a specific mechanism originating from the interconnected arms in the network, a very fast response with respect to UV photons can be obtained for photosensing applications.[1, 3] However, the larger dimensions of the C-FTS tetrapods (arm thickness ~ 1 µm, length ~ 10 µm) leads to a relatively poor gas sensing response for such 3-D network based devices.[3]

In this context, the formation of nano-heterojunctions proved to be a very efficient approach to drastically improve the gas response of semiconducting oxides nano- and microstructures.[9-10] For example, Park *et al.*[11] demonstrated a strategy for creating an air-bridge-structured CuO and ZnO nanowire array platform for achieving reliable distinction between H_2, CO and NO_2 gases. Choi *et al.*[9] reported on an excellent potential of ZnO-SnO_2 nanofiber-nanowire heterostructures for reproducible sensing of ppm level of NO_2 and CO gases by modulation of the potential barrier at heterojunctions interface. Also, highly sensitive H_2 gas sensors were elaborated for detection of sub-ppm level by using ZnO-SnO_2 nanofibers.[10] A bifunctional sensing mechanism was proposed to explain such ultra-high gas response, which includes the modulation of the potential barrier at SnO_2-SnO_2 interface and ZnO-SnO_2 heterojunction.[10] Also, the enhanced gas sensing properties of the non-planar *p-p*

(CuO/Cu_2O) heterojunctions with an excellent selectivity to ethanol vapour and to hydrogen gas after doping with Zn have been recently demonstrated by Lupan *et al.*[12-13] Thus, inspired by the expected higher efficiency of heterojunctions for more reliable and highly sensitive and selective gas detection, and also due to the possibility of combining a large variety of semiconducting oxides for formation of *n-n*, *n-p* and *p-p* heterojunctions, a new approach to fabricate ZnO-T-Me_xO_y and ZnO-T-$Zn_xMe_{1-x}O_y$ heterojunctions is investigated and proposed in the present work. By mixing the metal microparticles powder with ZnO-T using the C-FTS approach, different 3-D interconnected ZnO-T-Me_xO_y and ZnO-T-$Zn_xMe_{1-x}O_y$ hybrid networks were successfully obtained.[4] Morphological, structural, electrical and mechanical strength properties were reported in a previous article.[4]

In present work, we report for the first time on gas sensing performances of the ZnO-T-Fe_2O_3, ZnO-T-CuO and ZnO-T-$ZnAl_2O_4$ highly porous interconnected 3-D hybrid networks. Additionally, the possibility to considerably improve the gas response and to change/tune the gas selectivity of the ZnO-T networks is discussed based on the catalytic properties of the included metal oxides and the additionally formed potential barriers between the heterojunctions. The gas sensing studies revealed an enhanced selectivity of the ZnO-T-$ZnAl_2O_4$ hybrid networks with respect to H_2 and CH_4 gases, which is dependent on the Al concentration. The investigations demonstrated the possibility to tune/change the sensitivity from H_2 gas to ethanol vapour for ZnO-T-CuO, as well as to improve the response and selectivity with respect to CH_4 gas for ZnO-T-$ZnAl_2O_4$ networks with ratio 10:1. Calculations based on the density functional theory (DFT) have been performed to understand the interaction mechanisms between different gas molecules and the hybrid networks. Furthermore, a gas sensing mechanism based on the modulation of potential barriers at heterojunction interfaces has been developed.

2. EXPERIMENTAL SECTION

The Me_xO_y and $Zn_xMe_{1-x}O_y$ doped and alloyed ZnO-T hybrid networks with high porosity were obtained by mixing in different weight ratios ZnO-T (produced by C-FTS approach) with Me (Me = Fe, Cu, Al) and followed by subsequent thermal annealing in air in a furnace at 1150 °C for 5 h.[4] The produced samples were fully characterized by X-ray diffraction (XRD), micro-Raman, diffuse reflectance, photoluminescence (PL) and PL excitation (PLE) by using the experimental set-ups described in Supporting Information **Text S1**.

The sensor structures were fabricated according to the procedure described in a previous work.[3-4, 12-14] As above mentioned, before the integration of ZnO-T-Me_xO_y and ZnO-T-$Zn_xMe_{1-x}O_y$ (Me = Fe, Cu, Al) hybrid networks into the sensor structure, the as-produced samples were subjected to thermal annealing in an electrical furnace at 1150 ºC for 5 h in air. This process intends to promote a higher interconnectivity between the tetrapods and oxidize metal microparticles by attaching them firmly to the ZnO-T network. A width of 100 µm was used between the two gold contacts on a pre-patterned Au/Cr/glass template. The gas sensing measurement procedures were realized following the same procedure described in previous reported works.[3, 12-14] Concentration of all tested gases (H_2, ethanol vapour (EtOH), CO and CH_4) was 100 ppm, as in previous works. [3, 15] The relative humidity (RH) value during the measurements was set at normal ambient conditions of 30% RH, and was continuously measured by a standard hygrometer inside the test chamber. The gas response was calculated as the ratio between the electrical current under gas exposure (I_{gas}) and the electrical current through the sensor in the ambient air (I_{air}).

Computational Details

First-principles calculations on the Density Functional Theory (DFT) with the plane-wave pseudo-potential method [16-18] were performed, as implemented in the Vienna Ab-initio Simulation Package (VASP). [19] The projector augmented wave method was applied to describe the interaction between ions and electrons, [20] and the non-local exchange correlation energy was evaluated using the Perdew−Burke−Ernzerhof functional. [21] The geometry of atomic structures was optimised using the tetrahedron method with Blöchl correction [22] and the positions of all the atoms in the cell were fully relaxed until the atomic forces on each ion were less than 0.01 eV/Å. While modelling the interactions of the molecules with the surfaces, we used the implementation of the DFT-D2 approach described by Grimme [23] to account for long-range dispersion forces.

The bulk ZnO structure was modeled using an energy cut-off 400 eV and a 6×6×4 k-point grid by the Monkhorst-Pack method [24] for Brillouin zone sampling. For surface calculations, our model consists of six bilayers in which we have kept fixed the lower four bilayers in their optimized bulk positions to resemble the bulk material, while the atoms in the upper two bilayers were allowed to relax unconstrainedly to model the surface. A vacuum region of 12.5 Å was found to be sufficient to avoid interactions between periodic slabs in the

z-direction and a 3×3×1 *k*-point grid from the Monkhorst−Pack method [24] was determined to give converged data for the surface calculations.

The isolated molecules were modeled in the centre of individual broken symmetry cells with lattice constants of 20 Å, sampling just the gamma-point of the Brillouin zone with the uniform accuracy parameters as for the surfaces. The binding energy per molecule was computed from the relation $E_{ads} = E_{surf+mol} - (E_{surf} + E_{mol})$, where $E_{surf+mol}$ is the total energy of the adsorbate-substrate system, E_{surf} represents the energy of the naked surface slab, and E_{mol} is the energy of the isolated molecule. Within the definition, a negative binding energy shows an exothermic process.

3. RESULTS AND DISCUSSIONS

3.1. Morphology of ZnO-T-Me_xO_y and ZnO-T-$Zn_xMe_{1-x}O_y$ 3-D hybrid networks

The characterization of pristine ZnO-T networks was performed in detail in previous works[3-4] and by using the experimental set-ups described in Supporting Information **Text S1**. **Figure 1** illustrates scanning electron microscopy (SEM) images of the ZnO-T-Me_xO_y and ZnO-T-$Zn_xMe_{1-x}O_y$ (weight ratio of ZnO:Me is 10:1 and 20:1 respectively) highly porous and interconnected 3-D networks. For ZnO-T-Fe_2O_3 hybrid networks, the growth of randomly distributed nano- and microparticles on the surface of ZnO-T arms was observed-through the entire network of tetrapods (**Figure 1a,b** and **Figure S1**). The size of the tetrapods is in the range of 10 – 100 μm, while the diameter of the nano- and microparticles is in the range of 0.1 – 5 μm (for ZnO:Fe with weight ratio 20:1). The formation of interconnections among the arms of the tetrapods is depicted in **Figure S1a**. The hexagonal shape of arms of pristine ZnO tetrapods disappeared after doping-alloying with Fe (**Figure S1b**), and a more pronounced layered structure of the arms can be observed.[4] In case of ZnO-T-CuO (ZnO:Cu (20:1)) hybrid networks, a more evidenced change in morphology of the tetrapods was observed (**Figure 1c,d**). **Figure S2a,b** shows magnified SEM images of well-rounded interconnected arms with a smooth surfaces (the size of tetrapods is in the range of 20 – 150 μm). Unlike to what was observed for the ZnO-T-Fe_2O_3 samples, the growth of nano- and microparticles, such as for ZnO-T-Fe_2O_3 hybrid networks is absent in the case of ZnO-T-CuO hybrid networks, even for higher content of Cu (ZnO:Cu (10:1)) (**Figure S2c-d**). However, the growth of alloy-melt-like microstructures is observed on the surface of tetrapod arms, which actually leads to firm interconnection among the arms of tetrapods (**Figure S2c-f**). For ZnO-T-$ZnAl_2O_4$ (ZnO:Al (20:1) and (10:1)) hybrid networks an attractive layered morphology of the arms was observed (**Figure 1e,f**). The size of such tetrapods is in the range of 20 –

100 μm. Interconnections between various tetrapod arms are presented in **Figure S3**. As in the case of the ZnO-T-Fe_2O_3 3-D hybrid networks, a random distribution of microparticles with a rough surface was observed in the ZnO-T-$ZnAl_2O_4$ hybrid networks (**Figure S3b**). The diameter of these microparticles, which can form agglomerates, is up to 10 μm (**Figure 1e**).

To determine the origin of the second type of microstructures observed in the SEM images for all types of the network samples, compositional SEM images by energy dispersive X-ray (EDX) mapping were taken at microstructural level. As seen in **Figure S4**, the microspheres formed on the surface of ZnO-T with a mixture of ZnO:Fe (20:1) consist of Fe-oxide. In order to determine the crystal phase of the formed microspheres, further structural analysis was performed by X-ray diffraction (XRD) measurements. The diffractogram displayed in **Figure S5a,b** (for the sample ZnO-T-Fe_2O_3 after annealing at 1150 °C for 5 h) shows the main ZnO crystalline phase, in addition to different quantities of Fe_2O_3 maghemite and Fe_2O_3 hematite phases. The maghemite and Fe_2O_3 hematite phases are formed due to thermal reduction of the iron oxide, or they can also be obtained from the fully oxidized structures of Fe_2O_3 during the annealing process at high temperatures.[25] Based on the XRD data, it is quite difficult to clearly distinguish between different crystalline phases. Neverthless, the structural analysis evidences that the thermal annealing in air during 5 h at 1150 °C promotes the formation of the ZnO-T-Fe_2O_3 3-D hybrid ceramic networks. **Figure S5b** presents the X-ray diffraction patterns of the annealed ZnO-T-Fe_2O_3 network in zoomed-in for the 2θ range 25-45 degrees. It is seen that some ZnO and Fe_2O_3 diffraction maxima are close to each other or overlapped, making it challenging to full identify individual crystalline phases.

In a similar way to the ZnO-T-Fe_2O_3 network, compositional SEM images by energy EDX mapping were obtained for the ZnO-T-CuO and ZnO-T-$ZnAl_2O_4$ network samples with weight ratio of (20:1). From EDX mapping of the ZnO:Cu (20:1) and the ZnO:Al (20:1) network samples (see **Figure S6** and **Figure S7**, respectively) and the previously reported XRD analysis[4] it can be concluded that the formed microstructures were assigned to copper oxide and $ZnAl_2O_4$, respectively, forming ZnO-T-CuO and ZnO-T-$ZnAl_2O_4$ hybrid ceramic networks.

3.2. Photoluminescence and micro-Raman investigations on ZnO-T-Me_xO_y and ZnO-T-$Zn_xMe_{1-x}O_y$ 3-D hybrid networks

Photoluminescence (PL) spectroscopy was carried out to evaluate the optical active defects in the ZnO-T-Fe_2O_3, ZnO-T-CuO and ZnO-T-$ZnAl_2O_4$ hybrid networks. The presence

of bulk and surface defects and the balance between the recombination/trapping of the photo-generated carriers is known to be of upmost importance in the developed materials for gas sensing applications.[26-28] **Figure 2a** presents the room-temperature (RT) normalized PL spectra of the investigated samples which are mainly dominated by visible broad emission bands. Thus, for the formed hybrid ceramic networks the intensity of the near band edge emission (NBE) in the UV range at RT is considerably reduced compared to the visible luminescence. In the case of Al-alloyed-doped ZnO-T after thermal annealing of the networks at 1150 °C for 5 h, the formation of $ZnAl_2O_4$ is highly possible as per **Equation 1**:

$$ZnO + Al_2O_3 = ZnAl_2O_4 \quad (1)$$

where one monolayer of Al_2O_3 consumes one atomic layer of ZnO.[29-30] The formation of $ZnAl_2O_4$ crystalline phase was also confirmed by XRD measurements in our previous work.[4] Nevertheless, using photon excitation above the bandgap energies of both ZnO and $ZnAl_2O_4$ crystalline hosts (3.3 eV and 3.8 eV, respectively) no NBE from both materials was detected at RT.

The bands from the visible region are quite complex due to native, Me_xO_y and $Zn_xMe_{1-x}O_y$ induced defects in ZnO-T. Often, such broad unstructured emission bands in ZnO cover the blue, green, yellow, orange and red spectral zones[27, 31] and are frequently assigned to native defects such as oxygen vacancy (V_O),[32-33] zinc vacancy (V_{Zn}),[32] oxygen interstitials (O_i),[34] zinc interstitials (Zn_i) and their complexes.[27, 35] Moreover, the PL of the ZnO-T-$ZnAl_2O_4$ samples was shown to be strongly dependent on the excitation spot (plots (3) and (4) from **Figure 2a**) revealing that the optically active defects are inhomogeneously distributed. However, many groups have shown that the generated defects in ZnO micro- and nanostructures, as a cause of thermal annealing, doping, ball-milling treatment, etc., can greatly improve the gas, catalytic and UV sensing performances.[27-28, 36-37]

The samples' PL properties of the hybrid ceramic networks, ZnO-T-Me_xO_y and ZnO-T-$Zn_xMe_{1-x}O_y$, were further studied from 10 K to 300 K using above bandgap excitation as indicated in **Figure S8a-c**. With the used excitation conditions, and as commonly observed in bulk, thin films and ZnO micro- nanostructures, the vibronic assisted structured green emission was identified at low temperatures in all the studied networks, as displayed in **Figure 2b**. The green band is one of the most discussed optical centres in ZnO. The green structured band, usually associated with a Cu-related defect, exhibits two sets of longitudinal optical (LO, 72 meV) vibronic assisted progression with the main zero phonon lines (ZPLs)

separated by about 30 meV (ZPLs at 2.85 eV and 2.82 eV) due to the natural abundance of copper isotopes, as previously reported in the literature.[38-39] However, other explanations have been pointed out for the observation of the two vibronic progressions, such as the one proposed by Reynolds,[40] where a donor acceptor pair (DAP) recombination model (with a common deep acceptor and two distinct shallow donors) was considered as well as the participation of a local mode to assist the vibronic progression. Additionally, as it has been reported by Nobis *et al.*[41], ZnO micro- nanostructures are known to behave as optical resonators and spectral modulation of the visible defect-related broad bands through whispery gallery modes (WGM).[41]

As seen in **Figure 2b**, on the low energy side of the green emission other unstructured broad bands in the orange and red spectral regions were identified, namely for the Al-doped and Al-alloyed ZnO-T-$ZnAl_2O_4$ hybrid sample, showing that the emitting defects are inhomogeneously distributed in the synthesized network. The Fe-doped and ZnO-T-Fe_2O_3 samples exhibit a low energy shift for the peak position of the green emission with the main emission peaked at 2.2 eV, likely due to the overlap of emitting centers in the green, orange and red spectral zones. The PL intensity of the green spectral region was found to decrease with increasing temperatures being, however, dependent on the overlap degree with the low energy broad bands. More details on PL measurements are presented in **Figure S9**. Besides deep level emission, at low temperatures all the studied networks exhibit donor bound exciton emission in the UV spectral region. The PL intensity of all optically active defects thermally quenches with increasing temperature releasing free carriers that are expected to influence heterostructure band bending and, consequently, the gas sensing mechanisms.

The vibrational properties of ZnO-T can greatly influence the device performance.[26] Thus, micro-Raman measurements can provide useful information about material quality. **Figure 3** depicts the RT micro-Raman spectra of the studied samples. The spectra acquired for two different spots are shown for each sample. All the analysed samples indicate the typical vibrational modes close to the ZnO wurtzite structure.[42] It should be pointed out that second order Raman bands were observed in all the network samples, this process being typically activated by lattice disorder and resonant excitation conditions. The Cu-doped and ZnO-T-CuO hybrid networks show the most significant differences when different samples are being compared (**Figure 3b**). The spectra is dominated by an intense broad and assymetric band that is located at about 6 cm^{-1} below the expected value of the A_1(LO) of wurtzite ZnO. The great enhancement and the softening in the LO mode frequency indicated a scattering process mediated by a Frölich interaction under resonance conditions.[43] The frequencies of

the Frölich mediated mode can be tuned between the TO and LO frequencies and are strongly dependent on the environment of the host material lattice.[44-45] **Table S1** compares the vibrational frequencies observed in present work with those reported in the literature for wurtzite ZnO.[42]

3.3. RT diffuse reflectance and RT PLE investigations on ZnO-T-Me_xO_y and ZnO-T-$Zn_xMe_{1-x}O_y$ hybrid networks

Figure 4 shows the RT diffuse reflectance (left *y*-axis, dashed lines) and the RT PL excitation (PLE) spectra (right *y*-axis, full lines) monitored at the RT emission band maxima (**Figure 2a**) of the ZnO-T-Me_xO_y and ZnO-T-$Zn_xMe_{1-x}O_y$ structures. PLE spectra were only measured for the Fe- and Al-doped-alloyed ZnO-T samples, due to their higher emission intensity when compared to the remaining samples. ZnO is known to possess a direct bandgap of about 3.3 eV at RT[31, 46] and all analyzed samples exhibit a steeper absorption in the mentioned energy range. Nevertheless, both the PLE monitored for the PL emission maxima and the reflectance measurements indicate that below ZnO bandgap absorption occurs. This is very clear for the ZnO-T-Fe_2O_3 and ZnO-T-$ZnAl_2O_4$ doped and alloyed micro-nano-structures, where excitation shoulders/tail on the low energy part of the bandgap were identified by PLE. On the other hand, the reflectance measurements of the samples also revealed the band tails in the edge absorption region. Additionally, for the ZnO-T-Fe_2O_3 and ZnO-T-CuO hybrid networks, the subgap absorption bands can be clearly identified in the reflectance spectra. Fe-doped ZnO is known to exhibit subgap excitation[47-48] resulting in the well-structured red PL at low temperatures shown in **Figure 2b** and **S9a**. The most prominent identification is related with the ZnO-T-CuO hybrid networks where a broad ZnO subgap absorption band was identified in the reflectance spectra confirming that Raman scattering was performed under resonant conditions when the 442 nm (2.8 eV) laser line was used as excitation source, resulting in Raman spectra dominated by high intensity LO phonon mode as shown in **Figure 3b**. Since additional crystalline phases were promoted in the produced hybrid ZnO-T samples, at this stage we cannot rule out that the subgap absorption bands in the ZnO-T-CuO, ZnO-T-Fe_2O_3, and ZnO-T-$ZnAl_2O_4$ samples could also be related with bulk optical defects in the additional CuO, ZnO-T-Fe_2O_3, and $ZnAl_2O_4$ crystalline phases identified by XRD in the composites[4] and with the randomly distributed heterojunctions. Similarly, surface states could also contribute to observed absorption bands, located at lower energies than the ZnO energy band gap. If this is the case, these sates have high probability to be thermally populated at the sensor operating temperatures. As a consequence the surface

potential is changed, leading to a renormalization of the Fermi level and consequently the configuration of the energy bands at the interfaces of ZnO-T-Me_xO_y and ZnO-$Zn_xMe_{1-x}O_y$ can be dramatically modified affecting the charge transfer and consequently the amount of O^- adsorbated at the surface, influencing the behavior observed in the dependence of the gas response with the operating temperature. Therefore, the balance between the trapping and releasing of free carriers by the host defects, surface states and formed heterojunctions assumes an important role in the gas sensing properties.

3.4. Gas sensing properties of 3-D hybrid ceramic networks

Figure 5 shows the data on the gas response versus operating temperature (OPT) of the studied 3-D hybrid ceramic networks samples. For all samples, the typical bell-shape dependency of the gas response on operating temperature was observed which is strongly dependent on the type of adsorbed oxygen species on the surface of semiconducting oxides.[14, 49-50] At low operating temperatures (< 175 ºC) the gas response is relatively low due to insufficient thermal energy for the reaction of the tested gas molecules with the adsorbed oxygen species (in this temperature range mainly oxygen species O_2^- are adsorbed on the surface of metal oxides).[3, 49-51] With an increase in the operating temperature, the O_2^- are converted to O^- and the thermal energy is enough to overcome the activation energy barrier for the reaction of the tested gas molecules with the adsorbed O^-.[49, 51] However, with a further increase in temperature, the competing desorption of the adsorbed oxygen species leads to the decrease in gas response.[49] Different values of optimal operating temperatures in the investigated samples can be attributed to the different catalytic properties of the added materials (CuO, Fe_2O_3 and $ZnAl_2O_4$), which will be discussed in the gas sensing mechanism section.

The gas response of the sensors based on the ZnO-T-Fe_2O_3 (ZnO:Fe (20:1)) hybrid networks is presented in **Figure 5a**. The responses only to H_2 gas and ethanol vapour, with values of S_{H2} ~ 1.76 at an optimal OPT of 300 °C and a gas response S_{EtOH} ~ 2.1 at an optimal OPT of 250 °C have been detected. Thus, sensors based on the ZnO-T-Fe_2O_3 3-D hybrid networks haven't been further investigated due to their not so noticeable results compared to other Me_xO_y and $Zn_xMe_{1-x}O_y$ doped and alloyed ZnO-T and due to the low selectivity factor to ethanol vapour (S_{EtOH}/S_{H2} ~ 1.6 at OPT of 250 °C).

For the ZnO-T-CuO (ZnO:Cu (20:1)) hybrid networks based sensors, as in the case of ZnO-T-Fe_2O_3, only gas responses to H_2 gas and ethanol vapour were detected and the corresponding results are presented in **Figure 5b**. The optimal OPT for the H_2 gas sensing is

375 °C with S_{H2} ~ 2.37, while for ethanol vapours sensing is 350 °C with S_{EtOH} ~ 4.31. The selectivity factor for the ethanol vapour is S_{EtOH}/S_{H2} ~ 3.1, demonstrating a good selectivity of the ZnO-T-CuO hybrid networks for ethanol vapour sensing. In general, ethanol molecules (C_2H_5OH) react with chemisorbed oxygen from the surface of ZnO-T (**Equation (2)**) [9]:

$$C_2H_5OH(g) + 6O^-(ads) \rightarrow 2CO_2(g) + H_2O(g) + 6e^- \quad (2)$$

leading to a resistance decrease of *n*-type semiconducting oxides. In the case of samples with higher content of Cu (ZnO:Cu (10:1)) no significant gas response with *p*-type behaviour (resistance increased after introduction of reducing gases) was observed, see **Figure S10a**. Such samples were not further investigated further due to their high instability. This can be explained by the large amount of copper oxide that resulted onto the surface of ZnO-T that is being formed while CuO-alloying.[4] Due to specific surface conduction mechanism of *p*-type semiconducting oxides, the gas sensing mechanism is dominated by copper oxide.[12-14]

It can be observed from **Figure 5c**, that the highest gas response of ZnO-T-$ZnAl_2O_4$ (ZnO:Al (20:1)) hybrid networks was obtained for H_2 gas, S_{H2} ~ 7.5, at an OPT 250 °C. The gas response to CO, C_2H_5OH vapour and CH_4 gas was 1.3, 2.1 and 2.5, respectively. These results highlight the good selectivity to hydrogen gas of the ZnO tetrapod networks doped and alloyed with lower content of Al at an OPT of 250 °C. At exposure of the sensor to H_2 gas, the following reaction takes place (**Equation (3)**):[3]

$$2H_2(g) + 2O^-(ads) \rightarrow 2H_2O + 2e^- \quad (3)$$

Thus, the released electrons will contribute to a decrease in resistance of the *n*-ZnO-T networks.[9] The selectivity factors are S_{H2}/S_{CH4} ~ 2.26, S_{H2}/S_{EtOH} ~ 3.7 and S_{H2}/S_{CO} ~ 3.1 for ZnO-T-$ZnAl_2O_4$ (ZnO:Al (20:1)) hybrid networks. The optimal OPT for C_2H_5OH vapour sensing is 225 °C, which is lower than the optimal OPT for H_2 gas, but the ethanol vapour response is yet much lower than for H_2 gas (2.59 in comparison with 5.53, respectively). The optimal OPT for CH_4 gas is at 300 °C which is higher than the OPT for ethanol vapour and the H_2 gas detection regime, with a response of S ~ 3.21 for the investigated samples. This response is lower than that for H_2 gas (S ~ 6.2), at the respective OPT for the ZnO-T-$ZnAl_2O_4$ (ZnO:Al (20:1)) hybrid networks.

Figure 5d shows the gas sensing results for ZnO-T networks doped and alloyed with a higher content of Al (ZnO:Al (10:1)). The highest gas response was obtained for CH_4 gas, S_{CH4} ~ 28 at an OPT of 300 °C, while the gas response to CO, ethanol vapour and H_2 gas at the same OPT were 4.95, 4.0 and 4.6, respectively. Thus, by increasing the content of $ZnAl_2O_4$, the optimal OPT for CH_4 remained the same while for other tested gases it changed. These results highlight the change in selectivity from H_2 gas for ZnO:Al (20:1) to CH_4 gas for ZnO:Al (10:1) networks, by a significant increase in CH_4 gas response, from 2.5 to 28, respectively. The reaction process of CH_4 gas molecules with chemisorbed oxygen can be described by the following reaction (**Equation (4)**):[52]

$$CH_4(g) + 4O^-(ads) \rightarrow CO_2(g) + 2H_2O(g) + 4e^- \quad (4)$$

The selectivity factors for CH_4 gas at an OPT of 300 ˚C are S_{CH4}/S_{H2} ~ 6.1, S_{CH4}/S_{EtOH} ~ 7 and S_{CH4}/S_{CO} ~ 5.7 for ZnO-T-$ZnAl_2O_4$ (ZnO:Al (10:1)) hybrid networks. This is higher than for hydrogen in case of ZnO:Al (20:1). The gas response to ethanol vapours was increased from 2.13 to almost 9.85, while the optimal OPT for ethanol vapours was also increased from 225 °C to 350 °C, which is higher than the optimal OPT for other gases and it may help in improving the selectivity of sensors. The optimal OPT values for CO and H_2 gases at 275 °C are S_{H2} ~ 9.3 and S_{CO} ~ 13.7 for H_2 and CO gases, respectively. With a further increase in $ZnAl_2O_4$ content, the gas responses were lower than 1.5 for all type of gases and have not demonstrated any selectivity, thus were excluded from present investigations.

The gas response studies of Me_xO_y and $Zn_xMe_{1-x}O_y$ doped and alloyed ZnO-T networks based sensors are summarized in **Figure 6**, at their optimal operating temperature. It can be seen (**Figure 6**) that the ZnO:Al (20:1) samples are selective to hydrogen gas, the ZnO:Al(10:1) are selective to CH_4 gas, and ZnO:Cu (20:1) are selective to ethanol vapours. Such results clearly open up possibilities to tune/control the gas response of doped and alloyed ZnO-T 3-D networks with Me_xO_y and $Zn_xMe_{1-x}O_y$ (Me = Fe, Cu, Al) through developed technology. The optimal OPT variation for investigated samples was found to range between 250 °C and 350 °C. Thus, a change in selectivity of the ZnO-T hybrid networks based sensors by Me_xO_y and $Zn_xMe_{1-x}O_y$ alloying is demonstrated, revealing the high efficiency of this technological approach. In these studies, three types of sensing materials with excellent potential for the development of selective gas sensors were obtained and further integrated in to sensing device structures for selective detection of the three most

frequently used gases in the industry, biomedical and combustion systems, house environment, control of food quality, automobile industry, etc.

The influence of RH on gas sensing properties of ZnO-T-Me_xO_y and ZnO-T-$Zn_xMe_{1-x}O_y$ hybrid networks was also investigated. The fabricated sensors were tested at a higher RH value of 70%, using a bubbling system as reported previously.[12, 50] The obtained results are presented in **Figure 6** and **Table S3**. A decrease in gas response for all sensors was observed with an increase of the RH value to 70%. This can be explained by hydroxyl poisoning which results in a lower coverage of sensing material with oxygen species, and thereby lower electrical resistance and lower gas response.[9-10, 12, 50]

Next, transient responses of the sensors based on Me_xO_y and $Zn_xMe_{1-x}O_y$ (Me=Fe,Cu,Al) doped and alloyed ZnO-T hybrid networks have been analyzed. **Figure 7** shows the data on the gas sensing graphs of the CuO- and $ZnAl_2O_4$-alloyed hybrid ZnO-T networks based sensor structures. In the case of ZnO-T-CuO hybrid networks (see **Figure 7a**), the response (τ_r) and recovery (τ_d) times (defined as $\tau = |t_{90\%} - t_{10\%}|$) for ethanol vapors (*EtOH*) are 3.16 s and 2.8 s, respectively, while for H_2 gas are 16.7 s and 9.2 s, demonstrating a fast response and full recovery to the initial electrical baseline for *EtOH*. In the case of 70% RH, the rapidity of sensor structure decreased (see **Figure 7b**). The calculated response and recovery times for *EtOH* are τ_r = 4.5 s and τ_d = 4.3 s, while for H_2 gas are τ_r = 19.6 s and τ_d = 14.7 s. The ZnO:Al (20:1) samples demonstrated the lowest optimal OPT value of 250 °C with fast response and recovery times for all type of tested gases (see **Figure 6** and **Figure 7c,d**). For the H_2 gas response, the τ_r = 4.6 s and τ_d = 3.6 s for 30% RH and τ_r = 6.1 s and τ_d = 5.3 s for 70% RH (see **Figure 7d**) were obtained. In the case of *EtOH* sensing the τ_r = 4.8 s and τ_d = 4.3 s for 30% RH and τ_r = 6.7 s and τ_d = 6.2 s for 70% RH (see **Figure 7d**), demonstrating fully reversible response and excellent repeatability and stability. The τ_r for CO and CH_4 gases are 7.9 s and 5.8 s for 30% RH and τ_r = 8.9 s and τ_d = 7.1 s for 70% RH, while τ_d are 5 s and 6.2 s for 30% RH and τ_r = 7.1 s and τ_d = 8.9 s for 70% RH, respectively. Thus, as in the case of ZnO-T-CuO hybrid networks the rapidity of sensors was decreased with an increase in the RH value.

In the case of ZnO:Al (10:1) samples (with higher content of $ZnAl_2O_4$, see **Figure 7e,f**), the τ_r and τ_d for CH_4 gas response become much lower, taking 17.8 s and 21 s for the 90% of the full response and for the 10% recovery in the case of 30% RH. By increasing the RH value to 70% the τ_r increases to 21.8 s and τ_d increases to 29 s, showing the same tendency as in the case of other samples. In **Table S2** all data on gas response and recovery times are

summarized for all types of doped and alloyed Me_xO_y and $Zn_xMe_{1-x}O_y$ which are presented in **Figure 7**.

The gas response versus gas concentration (in ppm) of the tested gases was also investigated for hybrid networks (*EtOH* for ZnO:Cu (20:1), H_2 for ZnO:Al (20:1) and CH_4 for ZnO:Al (10:1)). The results are presented in **Figure S10b** (in the log *vs.* log plot). The respective slope (β) values were determined from linear fitting of the curves $\beta_{EtOH} = 0.45$, $\beta_{H2} = 0.41$ and $\beta_{CH4} = 0.63$. From **Figure S10b** the lowest detection limits (*LDL*) were estimated using the ratio $I_{gas}/I_{air} > 1.2$ criterion for gas detection, and the following results: $LDL_{EtOH} \approx 4$ ppm, $LDL_{H2} \approx 1$ ppm and $LDL_{CH4} = 0.7$ ppm.

Table 1 presents a comparison of the Me_xO_y and $Zn_xMe_{1-x}O_y$ doped and alloyed ZnO-T networks sensors parameters obtained in this work with those reported in the literature for doped and un-doped ZnO-T. It can be observed that the developed hybrid materials for sensors demonstrate faster rise/decay times in comparison with available specific data from **Table S2**.

3.5. Sensing mechanism proposed for ZnO-T-Me_xO_y and ZnO-T-$Zn_xMe_{1-x}O_y$ 3-D hybrid networks

Ionosorbtion based gas sensing mechanisms of a single and networked ZnO-T were reported in previous works.[1, 3, 53-54] Thus, to avoid repetition, here we been mainly focused on the influence of doped- and alloyed-hybrid ZnO-T networked structures on gas sensing properties. Due to annealing of the samples at 1150 °C for 5 h in order to reach higher interconnectivity of the tetrapods, the metal doped structures are fully oxidized, forming a second semiconducting oxide phase in the ZnO-T samples (Me_xO_y and/or $Zn_xMe_{1-x}O_y$), as was confirmed here by XRD results for ZnO-T-Fe_2O_3 hybrid networks as well as in a previous work involving other samples.[4]

The formation of heterojunctions for gas sensing applications is known to be a very efficient instrument to increase the gas sensing/response and to change/tune the selectivity.[12-13] For example by decoration of ZnO nanowire networks with nanocrystalline Co_3O_4 the gas response was enhanced due to catalytic effect of Co_3O_4.[55] Also, recently efficient *p-p* heterojunctions based on CuO and Cu_2O were elaborated by Lupan, *et al.* for efficient and reliable detection of ethanol vapours[13] or hydrogen gas by doping of copper oxides with Zn.[12] However, in our case the dimensions of ZnO-T are relatively high (in order of 1 – 100 μm), which can explain the relatively low gas sensing properties of pristine ZnO-T networks[3] compared to nano-ZnO-T networks.[1] The calculated approximate width of the electron

depleted region in pure ZnO was found to be in the range of 20 – 50 nm.[56-57] Thus, the local modulation of the electron depleted region of ZnO micro-structures by attaching another oxide phase cannot be the cause for the improvement of gas sensing properties to reducing gases of Me_xO_y and $Zn_xMe_{1-x}O_y$ doped and alloyed ZnO-T networks in the present work.

From the investigations in current and previous works,[4] it can be concluded that Me_xO_y and $Zn_xMe_{1-x}O_y$ are randomly dispersed in ZnO-T networks, forming multiple *p-n* (for ZnO-T-CuO) and *n-n* heterojunctions (for ZnO-T-$ZnAl_2O_4$ and ZnO-T-Fe_2O_3). The energy band diagram of the resulted heterojunctions in thermal equilibrium (**Figure S11**) are all of type II band alignment (staggered gap).[58] This type of band alignment is very efficient for electron and hole separation on different sides of heterojunctions.[58] The resulted potential barriers formed at these heterojunctions increase the sensors resistance, which has been already demonstrated by electrical measurements,[4] and it is consistent with literature results.[59-60] Thus, improved gas response properties of developed sensorial materials can be associated to additional modulation of resistance by potential barriers between *n-n* and *n-p* heterojunctions in hybrid networks, during adsorption and desorption of gaseous species from the surfaces (**Figure 8**).[9-10, 61-62]

At exposure of Me_xO_y and $Zn_xMe_{1-x}O_y$ doped and alloyed ZnO-T the air, oxygen molecules easily diffuse through the highly porous networks and adsorb on the surface of tetrapods and metal oxides by extracting electrons and forming potential barriers between ZnO-T arms and formed *n-n* (in the case of ZnO-T-$ZnAl_2O_4$ and ZnO-T-Fe_2O_3 hybrid networks) or *p-n* (in the case of ZnO-T-CuO) heterojunctions (**Figure 8a**).[9-10, 61-62] This leads to a lower current flow through the 3-D networks. During reducing gas exposure, the gas molecules interact with adsorbed oxygen species (**Equation (2-4)**) with a release of electrons,[9-10, 61-62] leading to a decrease of potential barriers (see **Figure 8b**). The poor gas response of the samples with higher content of CuO in ZnO-T-CuO hybrid networks can be explained by the formation of different microstructures agglomerations,[4] which considerably decrease the degree of porosity and surface-to-volume ratio of the samples, as well as the number of *p-n* heterojunctions, see **Figure S2c-f**. However, by using the concept of additionally created potential barriers between heterojunctions we cannot explain the differences in selectivity of the samples at the current stage. Pristine ZnO-T networks demonstrated good selectivity to H_2 gas[3] and in this work the change in selectivity by Me_xO_y and $Zn_xMe_{1-x}O_y$ alloying is demonstrated. The main reason could be the catalytic effect of the formed second metal oxide phase. Cu and Fe oxides are reported to be excellent catalysts for oxidation of volatile organic components (VOCs), in particular ethanol vapours.[13] This can

explain the higher selectivity to ethanol vapours of the ZnO-T-CuO and ZnO-T-Fe_2O_3 hybrid networks. In the case of ZnO-T-$ZnAl_2O_4$ hybrid networks, the lower content of $ZnAl_2O_4$ resulted in good selectivity to H_2 gas, while higher content of $ZnAl_2O_4$ leads to high selectivity to CH_4 gas. Thus, we can conclude that low content of $ZnAl_2O_4$ only enhance the H_2 gas response of the ZnO-T by additional created potential barriers, while higher content of $ZnAl_2O_4$ give rise to more accentuated catalytic reactions. Also, the layered morphology of these structures promotes a larger surface area of such networks, which lead to higher coverage with oxygen species. It is hard to obtain a clear image about gas sensing properties of $ZnAl_2O_4$ or $ZnAl_2O_4$-ZnO heterostructures, due to insufficient information in literature. $ZnAl_2O_4$ is known to be a good catalytic material with 3.8 eV optical bandgap[63] and high thermal and chemical stability.[64] Methane gas is the most difficult hydrocarbon fuel to be oxidized.[64] However, recent results demonstrated good catalytic results of Ru/$ZnAl_2O_4$ for total oxidation of methane.[64] Therefore, we strongly believe that the demonstrated $ZnAl_2O_4$-ZnO heterojunction is a good candidate for selective detection of hydrocarbons and more studies are needed to elucidate gas sensing properties of this type of heterojunction.

Compared to other results on gas sensor based on ZnO-T networks (see Table 1), our sensors posses relatively high rapidity (shorter response/recovery time). In general, the high rapidity of tetrapod networks can be explained based on their anti-agglomeration properties which lead to high porosity with micrometric pores for quick diffusion of gas molecules and oxygen species (by molecular diffusion).[3] However, in our case the improved rapidity can be explained based on the same principles as in the case of changed selectivity, i.e. taking into account the catalytic effects of added Me_xO_y and $Zn_xMe_{1-x}O_y$. Because the response and recovery reactions are dependent on in-diffusion/adsoprtion/ionization of oxygen, and oxidation of tested gas molecules (**Equation (2-4)**), the high rapidity of hybrid structures can be attributed to the promotion of these surface reactions by the presence of Fe_2O_3, CuO and $ZnAl_2O_4$.[59-61, 65]

3.6. DFT study of H_2, CO, CH_4 and ethanol gas molecule interactions on Fe_2O_3, CuO and Al_2O_4 doped ZnO(0001) surfaces

3.6.1. ZnO Bulk and ZnO(0001) Surface

We first optimized the bulk wurtzite ZnO structure and found calculated lattice parameters of a = 3.2552 Å and c = 5.2396 Å, which match well with the experimental values[66] of a = 3.2496 Å, c = 5.2901 Å and are in better agreement than an earlier theoretical study.[67] The Zn-terminated polar (0001) surfaces have been found to be the active ZnO

surfaces for the adsorption of gas molecules and other surface reactions.[68-69] We therefore modeled this surface to understand the doped ZnO tetrapods and their interaction with different gas molecules. In order to quench the macroscopic dipole associated with a non-reconstructed bulk-terminated (0001) polar surface, the ZnO crystal was cleaved along the (0001) plane and every fourth Zn atom from the top and every fourth O atom from the bottom of the slab.[68-69] The reconstructed surface cell then consists of 23 Zn and 23 O atoms in a 2×2 supercell, where the topmost layer incorporates of 3 Zn and 4 O atoms (**Figure S12**) and each Zn atom is bound to three oxygen atoms with bond lengths of 1.885 and 1.939 Å.

3.6.2. Fe_2O_3:ZnO(0001) Surface

In order to model the Fe_2O_3:ZnO(0001) surface, the three Zn atoms were replaced with two Fe atoms by considering a number of structures with Fe atoms substituting Zn atoms in the first and second bilayers. Among the different substituted structures investigated, the most stable one had all three top layer Zn atoms replaced by the Fe atoms. In the relaxed structure, each Fe atom binds to three oxygens, connecting with two oxygens with a bond length of 1.796 Å and to one another oxygen at 1.681 Å (**Figure S13**).

H_2 adsorption at the Fe_2O_3-doped ZnO (0001) surface was investigated by placing the H_2 molecule close to different surface atoms in parallel and perpendicular direction to the surface in a series of different initial configurations. We found that the H_2 molecule dissociates and binds to one of the surface O atoms, thereby forming a surface-bound water molecule. During the formation of this water molecule, the bond between the surface O atom and an Fe atom breaks, while its bond with a Zn atom in the second layer is stretched from 1.972 to 2.061 Å (**Figure S14a,b**). The O-H bond lengths for the two hydrogen atoms are found to be 0.986 and 1.007 Å, indicating that one of the H atoms approaches a neighbouring surface oxygen atom. The connection/interaction of the H_2 molecule with the surface releases 308.8 kJ/mol, showing the adsorption process to be a strongly exothermic reaction.

The interaction of the CO gas molecule with the Fe_2O_3:ZnO(0001) surface was studied by placing it near the top layer surface atoms, as well as near the Zn atoms in the second layer. During molecule-surface interaction, the C atom binds to a surface Fe atom with a bond length of 1.971 Å, whereas it also connects with a surface oxygen atom with a bond length of 1.228 Å. The molecule binds to the surface oxygen atom to form a bent surface-bound CO_2 molecule, as a shown in **Figure S14c,d**. The surface Fe atom, which was bonded to three surface oxygen atoms, breaks its bond to this O atom (i.e. the one that became bound to the C

atom of CO) and elongates its bonds to the other two oxygen atoms to 1.801 Å, from their initial values of 1.795 Å. The binding energy calculated for the CO molecule is -196.9 kJ/mol.

Next, we placed the CH_4 molecule close to the Fe and O surface atoms in a number of different initial positions and orientations, and found that no chemisorption of the molecule occurs on the Fe_2O_3:ZnO(0001) surface. The most stable configuration found was one, in which the CH_4 molecule is physisorbed with a binding energy of just -24.6 kJ/mol, shown in **Figure S14e,f**. The physisorption of CH_4 is also reflected in terms of structural changes, as one of the H-C-H angle reduces to 107.5° from its original value of 109.5°, whereas surface Fe-O bonds stretch slightly from 1.796 Å to 1.824 and 1.822 Å and from 1.681 Å to 1.694 Å.

In all the optimized adsorbed modes of the ethanol molecule from a range of initial starting configurations, the molecule binds to surface Fe atoms through its O atom. The most stable configuration is shown in **Figure S14g,h**, where the ethanol molecule's O atom binds to the surface Fe atom at a distance of 2.017 Å. The surface Fe-O bonds stretch, extending to 1.846, 1.831 and 1.705 Å. The binding energy calculated for this configuration is -143.5 kJ/mol. A similar binding is observed through a second surface Fe atom in the top layer.

3.6.3. CuO:ZnO(0001) Surface

We modeled the CuO:ZnO(0001) surface by substituting one Zn atom by one Cu atom in the ZnO(0001) surface and determined the most stable doped surface by replacing different surface Zn atoms in the first and second layer. In the relaxed structure, Cu atoms prefer to be in the topmost surface layer (**Figure S15**). We did not observe any surface reconstruction as a result of this Cu substitution, whereas the Cu atom bonds to three surface O atoms, similar to the structural bonding in the pristine ZnO(0001) surface. The bond lengths of two Cu-O bonds are 1.843 Å, while the other Cu-O bond length is 1.940 Å.

The interaction of the H_2 gas molecule with the CuO:ZnO(0001) surface was investigated by placing the H_2 molecule close to surface Zn, O and Cu atoms in various possible orientations. It was observed that by placing the H_2 molecule close to the Cu atom and those O atoms bonded to Cu, the molecule dissociates and binds to two oxygen atoms, as shown in **Figure S16a,b**. This process is similar to that found on the Cu(I) oxide and Zn-doped Cu(I) oxide surfaces, where the H_2 molecule dissociatively binds to the surface.[50, 70] The dissociated hydrogen atoms connect with two surface oxygens with bond lengths of 1.024 and 0.981 Å and, as a result of this hydrogen adsorption, the bond between Cu and one such oxygen is broken, whereas the Cu connects to a nearby Zn atom through a weak Zn-C bond of 2.771 Å. The binding energy calculated for the H_2 gas molecule interaction is -181.8 kJ/mol.

The CO molecule binds to surface O and Cu atoms through the formation of C-Cu and C-O bonds of lengths 1.891 and 1.332 Å, respectively. As a result of these interactions of the CO molecule with surface O atoms, the Cu-O bond to this surface oxygen is broken and the other two Cu-O bonds are elongated to 1.858 and 1.941 Å, while the intramolecular C-O bond is found to be 1.212 Å (**Figure S16c,d**). The interaction of the CO molecule with the CuO:ZnO(0001) surface releases an energy of 101.7 kJ/mol.

Similar to the process on the Fe_2O_3:ZnO(0001) surface, the CH_4 molecule shows no chemisorption with the CuO:ZnO(0001) surface, where it interacts only weakly with a binding energy of just -28.6 kJ/mol (**Figure S16e,f**). The molecule stays above the surface at ~2.420 Å. As a result of this CH_4 interaction, the surface Cu-O bond lengths change to from 1.813 Å to 1.902 and 1.813 Å and from 1.940 Å to 1.932 Å.

The ethanol molecule binds in a similar fashion as on Fe_2O_3:ZnO(0001) surface, but less strong (**Figure S16g,h**). The molecule interactions with the surface atoms releases the energy of 107.5 kJ/mol, where the oxygen atom of the molecule connects with the Cu dopant atom, forming a O-Cu bond of 2.022 Å. The Cu atom moves up to connect with the molecule, thereby increasing one of the Cu-O bonds in the surface to 2.031 from 1.940 Å, while the other Cu-O bonds elongate from 1.843 Å to 1.906 Å and 1.868 Å.

3.6.4. Al_2O_4:ZnO(0001) surface

One Al atom was substituted for two Zn atoms in the ZnO(0001) surface to model the Al_2O_4:ZnO(0001) surface. We tried different configurations by replacing Zn atoms in the first and second layers and found that in contrast to CuO and Fe_2O_3 doped surfaces, the Al atom prefers to be in the second bilayer. The most stable Al_2O_4:ZnO(0001) surface structure is shown in **Figure S17a,b** (named as configuration A), where one Al atom was substituted for two Zn atoms in the second bilayer. The Al dopant atom connects with one O atom in the top later, $d_{O\text{-}Zn}$ = 1.785 Å, and two oxygens in the second layer with length of bond of 1.775 and 1.787 Å. The optimized geometry consists of three Zn atoms in the top layer, each bonded to three O atoms with bond lengths varying from 1.835 to 1.950 Å. A similar stable configuration is shown in **Figure S17c,d**, where a Zn atom has moved to the second layer and the Al connects to two O atoms below ($d_{Al\text{-}O}$ = 1.846 Å) and one O atom in the top layer ($d_{Al\text{-}O}$ = 1.726 Å). This configuration (noted as configuration B) is found to be negligibly more stable (by only 0.006 eV) than configuration A.

We first calculated the interaction of the H_2 molecule with surface configuration A, by placing the molecule close to different surface atoms, including the Al dopant atom in the

second bilayer. The most stable structure is found by placing the H_2 molecule on top of a surface oxygen atom which is bonded with the Al atom. It was observed that the H_2 molecule dissociates and binds atomically with the surface oxygen atoms, while the Zn atom in the top layer which was bonded with these surface O atoms, moves down to the second layer and changes the surface structure to surface configuration 2 (**Figure 9a,b**). The Al-O bond length increases from 1.785 Å to 1.799 Å, while the O atom binds to the Zn atom with a bond length of 2.004 Å. Here, the H_2 molecule interacts strongly with the surface, releasing -388.8 kJ/mol of energy. We also investigated interaction of the H_2 molecule on the second surface configuration (configuration B) and found that the molecule again dissociates, with one H atom connecting with the O atom bonded to the Al below, while the second H atom binds to a nearby top surface O atom. In result of the adsorption of the H_2 molecule, the surface structure changes to the configuration A structure, with a Zn atom in the top layer. The binding energy calculated for this surface configuration is about -382 kJ/mol, indicating a similar strength of adsorption. Hence, for the interactions of the CO, CH_4 and ethanol molecules, we have considered only surface configuration A.

When we placed the CO molecule near the O-Al bond, it adsorbs on the Al_2O_4:ZnO(0001) surface by connecting with the surface oxygen atom through a C-O bond of 1.339 Å. The molecule also binds with one of the surface Zn atoms at a distance of 2.017 Å. Here also, as a result of interactions between the molecule and the surface oxygen atom, the Zn surface atom moves down and occupies the place of a Zn vacancy, converting to surface configuration 2, as shown in **Figure 9c,d**. The surface O atom moves up to connect to the C atom of the molecule whilst elongating the Al-O bond length to 1.796 Å. The binding energy shows that the molecule interacts strongly with the Al_2O_4:ZnO(0001) surface, releasing an adsorption energy of 383.5 kJ/mol.

Similar to the other doped surfaces, the methane molecule shows no chemisorption on the Al_2O_4:ZnO(0001) surface. The most stable configuration is shown in **Figure 9e,f**, where the molecule interacts weakly with the surface at a distance of ~2.8 Å away from the Zn-O bond connected to the Al dopant atom below. As a result of this weak molecule-surface interaction, the length of this Zn-O bond increases slightly from 1.919 Å to 1.927 Å. The calculated binding energy is -34.2 kJ/mol, which is slightly larger than the adsorptions on the Fe_2O_3:ZnO and CuO:ZnO(0001) surfaces.

The interaction of the ethanol molecule with the Al_2O_4:ZnO(0001) surface was investigated by placing the molecule near all surface atoms in various possible orientations. It was observed that the molecule dissociates and binds to the surface as a CH_3OCH fragment,

with its O atom connecting to a surface Zn atom with a bond length of 2.031 Å. The other two H atoms bind to two surface O atoms, with bond lengths of 0.983 and 0.990 Å (**Figure 9g,h**). The Zn atom moves up to connect to the O atom of the molecule by stretching three surface Zn-O bonds to 1.989, 1.941 and 1.970 Å. The calculations show that an energy of 418.5 kJ/mol is released due to the adsorption of the ethanol molecule at the Al_2O_4:ZnO(0001) surface. We have summarized the binding energies of different molecules on Fe_2O_3:ZnO(0001), CuO:ZnO(0001) and Al_2O_4:ZnO(0001) surfaces in **Table S4**. The binding energy values show that all the gas molecules interact strongly on Al_2O_4 doped surfaces compared to interaction on Fe_2O_3 and CuO doped surfaces.

Present DFT calculations provide fundamental understanding at ideal ZnO surfaces at 0 K temperature, which are still relevant for applications at elevated temperatures. Although, higher binding of the molecules not necessarily means the better sensing, however this could be one of the indicators of the gas molecule sensing on these doped ZnO surfaces.

4. CONCLUSION

Me_xO_y and $Zn_xMe_{1-x}O_y$ (Me=Fe, Cu, Al) doped and alloyed ZnO-T 3-D hybrid networks were synthesized by a simple FTS approach followed by thermal annealing and were subsequently integrated in sensors. The samples were studied by SEM, XRD, PL, Raman and sensing techniques and were supported by DFT computation indicating on doping and alloying of ZnO-T with Fe, Cu or Al. XRD confirmed the formation of hybrid networks from crystalline Me_xO_y and $Zn_xMe_{1-x}O_y$ doped and alloyed ZnO-tetrapods. The main observed vibrational modes detected Raman spectroscopy are due to the wurtzite structure of the ZnO-T. Resonant Raman modes were promoted in the ZnO-T-CuO network under below ZnO bandgap excitation in agreement with the presence of sub bangap absorption bands as observed by diffuse reflectance and photoluminescence excitation. The sub bangap absorption bands, present in all the networks, are likely due the formed heterojunctions and surface states which influencing further response on the gas sensing. Additionally, we cannot discard that bulk defects induced by the doping of ZnO and/or optical defects present in secondary crystalline phases of copper oxide, iron oxide, and zinc aluminate, also could be contributing to the sub band gap absorption bands. The photoluminescence properties of the networks clearly reveal the presence of optically active defects. In particular, at low temperatures the main emission is due to the bound exciton and deep level recombination on ZnO host (structured green emission, unstructured red band and intraionic Fe^{3+} in the ZnO-T-Fe_2O_3 network). The latter is the dominant emission at room temperature. The optically active centers in the networks were found to be inhomogeneously distributed as shown for the case of the ZnO-T-$ZnAl_2O_4$ network.

The obtained highly porous hybrid networks exhibit improved reducing gas sensing properties in comparison with pristine ZnO-T. SEM studies revealed modifications of the tetrapods morphology induced by Me_xO_y- and $Zn_xMe_{1-x}O_y$-alloying, and the formation of different randomly distributed Me_xO_y and $Zn_xMe_{1-x}O_y$ microstructures on ZnO-T surfaces. Me_xO_y and $Zn_xMe_{1-x}O_y$ have formed after thermal annealing at 1150 °C for 5 h, which was applied to form interconnected networks, were found to be a crucial factor for the improvement of sensing properties of the hybrid networks. Additional formed *n-n* and *n-p* heterojunctions lead to a more efficient modulation of the sensor resistance during adsorption and desorption of gaseous species. ZnO-T-Fe_2O_3 and ZnO-T-CuO hybrid networks

demonstrated higher gas response to ethanol vapour, while ZnO-T-$ZnAl_2O_4$ hybrid networks demonstrated good selectivity to H_2 gas (for ZnO:Al (20:1)) and to CH_4 (for ZnO:Al (10:1)). The change in selectivity was attributed to catalytic properties of the Me_xO_y and $Zn_xMe_{1-x}O_y$. The gas sensing mechanism was studied in detail based on the potential barrier modulation between formed *n-n* and *n-p* heterojunctions during surface adsorption of oxygen atoms and oxidizing of the tested gas molecules. In line with experimental findings, DFT calculations showed that ZnO-T-Al_2O_4 are better hybrid networks with respect to gas sensing, since the Al_2O_4 doped ZnO(0001) surfaces demonstrate stronger interactions with the different gases than the other two systems. Achieved results clearly demonstrate new possibilities to tune and control the gas sensing response of ZnO-T networks by doping and alloying with Fe, Cu or Al metals and to provide better sensors for industrial and environmental monitoring. Such materials can be used for further fundamental and experimental studies.

■ ASSOCIATED CONTENT

Supporting Information: Experimental section on optical and structural measurements. Figures showing SEM images, compositional images taken by EDX elemental mapping at the microstructural level, temperature dependent PL spectra, normalized (at 2.4 eV) intra-shell Fe^{3+} PL observed at 10 K of Me_xO_y and $Zn_xMe_{1-x}O_y$ doped and alloyed ZnO-T hybrid networks. Figures showing the X-ray diffraction patterns of the ceramics from ZnO-T-Fe_2O_3 samples, transient ethanol vapour response of the sensors based on ZnO-T-CuO (ZnO:Cu (10:1)) hybrid networks at 275 ºC operating temperature and schematic energy band diagram of the *n*-Fe_2O_3/*n*-ZnO-T, p-CuO/*n*-ZnO-T and *n*-$ZnAl_2O_4$/*n*-ZnO-T heterojunction in the thermal equilibrium and a Table showing vibrational frequencies observed in this work. Also, figures related to DFT study and a table with values of binding energies of different gas molecules on metal oxides surface. The Supporting Information is available free of charge on the ACS Publications website at http://pubs.acs.org

■ AUTHOR INFORMATION

Corresponding Author

*E-mail: ollu@tf.uni-kiel.de ra@tf.uni-kiel.de

Notes

The authors declare no competing interest.

ACKNOWLEDGMENT

Dr. Lupan acknowledges the Alexander von Humboldt Foundation for the research fellowship for experienced researchers 3-3MOL/1148833 STP at the Institute for Materials Science, University of Kiel, Germany. The authors acknowledge the support from German Research Foundation (DFG) under the scheme PAK 902 (AD 183/16-1, AD 183/17-1) and by Project SFB859. Additionally, part of the work was funded by FEDER funds through the COMPETE 2020 Programme and FCT (Portuguese Foundation for Science and Technology) funds through the projects UID/CTM/50025/2013 and RECI-II/FIS-NAN/0183/2012 (FCOMP-01-0124-FEDER-027494). Dr. A K. Mishra and Prof. Nora H. de Leeuw acknowledge the Engineering and Physical Sciences Research Council (EPSRC) "4CU" programme grant (EP/K001329/1 and EP/K035355/1). Prof. de Leeuw also thanks the Royal Society for an Industry Fellowship. A.K.M. also acknowledges the startup (SEED) grant from the University of Petroleumand Energy Studies (UPES), Dehradun, India. This research was partly supported by the project Institutional 45inst-15.817.02.29A funded by the Gouvernment of the Republic of Moldova.

■ REFERENCES

(1) Gedamu, D.; Paulowicz, I.; Kaps, S.; Lupan, O.; Wille, S.; Haidarschin, G.; Mishra, Y. K.; Adelung, R. Rapid Fabrication Technique for Interpenetrated ZnO Nanotetrapod Networks for Fast UV Sensors. *Adv. Mater.* **2014,** *26*, 1541-1550.
(2) Hölken, I.; Neubüser, G.; Postica, V.; Bumke, L.; Lupan, O.; Baum, M.; Mishra, Y. K.; Kienle, L.; Adelung, R. Sacrificial Template Synthesis and Properties of 3-D Hollow-Silicon Nano-and Microstructures. *ACS Appl. Mater. Interfaces* **2016,** *8*, 20491-20498.
(3) Mishra, Y. K..; Modi, G.; Cretu, V.; Postica, V.; Lupan, O.; Reimer, T.; Paulowicz, I.; Hrkac, V.; Benecke, W.; Kienle, L.; Adelung, R. Direct Growth of Freestanding ZnO Tetrapod Networks for Multifunctional Applications in Photocatalysis, UV Photodetection, and Gas Sensing *ACS Appl. Mater. Interfaces* **2015,** *7* (26), 14303-14316.
(4) Gröttrup, J.; Paulowicz, I.; Schuchardt, A.; Kaidas, V.; Kaps, S.; Lupan, O.; Adelung, R.; Mishra, Y. K. Three-Dimensional Flexible Ceramics Based on Interconnected Network of Highly Porous Pure and Metal Alloyed ZnO Tetrapods. *Ceram. Int.* **2016,** *42*, 8664-8676.
(5) Postica, V.; Hölken, I.; Schneider, V.; Kaidas, V.; Polonskyi, O.; Cretu, V.; Tiginyanu, I.; Faupel, F.; Adelung, R.; Lupan, O. Multifunctional Device Based on ZnO: Fe Nanostructured Films with Enhanced UV and Ultra-Fast Ethanol Vapour Sensing. *Mater. Sci. Semicon. Proc.* **2016,** *49*, 20-33.
(6) Lupan, O.; Chow, L.; Chai, G.; Heinrich, H. Fabrication and Characterization of Zn–ZnO Core–Shell Microspheres from Nanorods. *Chem. Phys. Lett.* **2008,** *465*, 249-253.
(7) Reimer, T.; Paulowicz, I.; Röder, R.; Kaps, S.; Lupan, O.; Chemnitz, S.; Benecke, W.; Ronning, C.; Adelung, R.; Mishra, Y. K. Single Step Integration of ZnO Nano- and Microneedles in Si Trenches by Novel Flame Transport Approach: Whispering Gallery Modes and Photocatalytic Properties. *ACS Appl. Mater. Interfaces* **2014,** *6*, 7806-7815.
(8) Lupan, O.; Guérin, V. M.; Ghimpu, L.; Tiginyanu, I. M.; Pauporté, T. Nanofibrous-Like ZnO Layers Deposited by Magnetron Sputtering and Their Integration in Dye-Sensitized Solar Cells. *Chem. Phys. Lett.* **2012,** *550*, 125-129.
(9) Choi, S.-W.; Katoch, A.; Sun, G.-J.; Kim, S. S. Synthesis and Gas Sensing Performance of ZnO–SnO_2 Nanofiber–Nanowire Stem-Branch Heterostructure. *Sens. Actuators B* **2013,** *181*, 787-794.
(10) Katoch, A.; Kim, J.-H.; Kwon, Y. J.; Kim, H. W.; Kim, S. S. Bifunctional Sensing Mechanism of SnO_2–ZnO Composite Nanofibers for Drastically Enhancing the Sensing Behavior in H_2 Gas. *ACS Appl. Mater. Interfaces* **2015,** *7*, 11351-11358.

(11) Park, W. J.; Choi, K. J.; Kim, M. H.; Koo, B. H.; Lee, J.-L.; Baik, J. M. Self-Assembled and Highly Selective Sensors Based on Air-Bridge-Structured Nanowire Junction Arrays. *ACS Appl. Mater. Interfaces* **2013,** *5*, 6802-6807.
(12) Lupan, O.; Cretu, V.; Postica, V.; Polonskyi, O.; Ababii, N.; Schütt, F.; Kaidas, V.; Faupel, F.; Adelung, R. Non-Planar Nanoscale p-p Heterojunctions Formation in $Zn_xCu_{1-x}O_y$ Nanocrystals by Mixed Phases for Enhanced Sensors. *Sens. Actuators B* **2016,** *230C*, 832-843.
(13) Lupan, O.; Cretu, V.; Postica, V.; Ababii, N.; Polonskyi, O.; Kaidas, V.; Schütt, F.; Mishra, Y. K.; Monaico, E.; Tiginyanu, I.; Sontea, V.; Strunskus, T.; Faupel, F.; Adelung, R. Enhanced Ethanol Vapour Sensing Performances of Copper Oxide Nanocrystals with Mixed Phases. *Sens. Actuators B* **2016,** *224*, 434-448.
(14) Lupan, O.; Postica, V.; Cretu, V.; Wolff, N.; Duppel, V.; Kienle, L.; Adelung, R. Single and Networked CuO Nanowires for Highly Sensitive p-type Semiconductor Gas Sensor Applications. *Phys. Status Solidi RRL* **2015,** *10*, 260-266.
(15) Chai, G. Y.; Lupan, O.; Rusu, E. V.; Stratan, G. I.; Ursaki, V. V.; Şontea, V.; Khallaf, H.; Chow, L. Functionalized Individual ZnO Microwire for Natural Gas Detection. *Sens. Actuators A* **2012,** *176*, 64-71.
(16) Kresse, G.; Hafner, J. Ab initio Molecular Dynamics for Liquid Metals. *Phys. Rev. B* **1993,** *47*, 558.
(17) Kresse, G.; Furthmüller, J. Efficient Iterative Schemes for *ab initio* Total-Energy Calculations Using a Plane-Wave Basis Set. *Phys. Rev. B* **1996,** *54*, 11169-11186.
(18) Kresse, G.; Furthmüller, J. Efficiency of *ab initio* Total-Energy Calculations for Metals and Semiconductors Using a Plane-Wave Basis Set. *Comp. Mater. Sci.* **1996,** *6*, 15-50.
(19) Kresse, G.; Hafner, J. Ab initio Molecular-Dynamics Simulation of the Liquid-Metal–Amorphous-Semiconductor Transition in Germanium. *Phys. Rev. B* **1994,** *49*, 14251.
(20) Blöchl, P. E. Projector Augmented-Wave Method. *Phys. Rev. B* **1994,** *50*, 17953.
(21) Perdew, J. P.; Burke, K.; Ernzerhof, M. Generalized Gradient Approximation Made Simple. *Phys. Rev. Lett.* **1996,** *77*, 3865.
(22) Blöchl, P. E.; Jepsen, O.; Andersen, O. K. Improved Tetrahedron Method for Brillouin-Zone Integrations. *Phys. Rev. B* **1994,** *49*, 16223.
(23) Grimme, S. Semiempirical GGA-type Density Functional Constructed with a Long-Range Dispersion Correction. *J. Comp. Chem.* **2006,** *27*, 1787-1799.
(24) Monkhorst, H. J.; Pack, J. D. Special Points for Brillouin-Zone Integrations. *Phys. Rev. B* **1976,** *13*, 5188.
(25) Cannas, C.; Gatteschi, D.; Musinu, A.; Piccaluga, G.; Sangregorio, C. Structural and Magnetic Properties of Fe_2O_3 Nanoparticles Dispersed over a Silica Matrix. *J. Phys. Chem. B* **1998,** *102*, 7721-7726.
(26) Lupan, O.; Ursaki, V. V.; Chai, G.; Chow, L.; Emelchenko, G. A.; Tiginyanu, I. M.; Gruzintsev, A. N.; Redkin, A. N. Selective Hydrogen Gas Nanosensor Using Individual ZnO Nanowire with Fast Response at Room Temperature. *Sens. Actuators B* **2010,** *144*, 56-66.
(27) Ursaki, V. V.; Lupan, O. I.; Chow, L.; Tiginyanu, I. M.; Zalamai, V. V. Rapid thermal annealing induced change of the mechanism of multiphonon resonant Raman scattering from ZnO nanorods. *Solid State Commun.* **2007,** *143*, 437-441.
(28) Shishiyanu, S. T.; Lupan, O. I.; Monaico, E. V.; Ursaki, V. V.; Shishiyanu, T. S.; Tiginyanu, I. M. Photoluminescence of chemical bath deposited ZnO:Al films treated by rapid thermal annealing. *Thin Solid Films* **2005,** *488*, 15-19.
(29) Hou, Q.; Meng, F.; Sun, J. Electrical and Optical Properties of Al-doped ZnO and $ZnAl_2O_4$ Films Prepared by Atomic Layer Deposition. *Nanoscale Res. Lett.* **2013,** *8*, 1-8.
(30) Chen, X. Y.; Li, J. H.; Sun, Z. H.; Fang, X.; Wei, Z. P.; Fang, F.; Chu, X. Y.; Li, S.; Wang, X. H. The Formation and Acceptor Related Emission Behavior of $ZnO/ZnAl_2O_4$ Core–Shell Structures. *J. Alloy. Compd.* **2013,** *571*, 114-117.

(31) Özgür, Ü.; Alivov, Y. I.; Liu, C.; Teke, A.; Reshchikov, M. A.; Doğan, S.; Avrutin, V.; Cho, S.-J.; Morkoç, H. A Comprehensive Review of ZnO Materials and Devices. *J. Appl. Phys.* **2005,** *98*, 041301.
(32) Guo, B.; Qiu, Z. R.; Wong, K. S. Intensity Dependence and Transient Dynamics of Donor–Acceptor Pair Recombination in ZnO Thin Films Grown on (001) Silicon. *Appl. Phys. Lett.* **2003,** *82*, 2290-2292.
(33) Vanheusden, K.; Warren, W. L.; Seager, C. H.; Tallant, D. R.; Voigt, J. A.; Gnade, B. E. Mechanisms Behind Green Photoluminescence in ZnO Phosphor Powders. *J. Appl. Phys.* **1996,** *79*, 7983-7990.
(34) Wu, X. L.; Siu, G. G.; Fu, C. L.; Ong, H. C. Photoluminescence and Cathodoluminescence Studies of Stoichiometric and Oxygen-Deficient ZnO Films. *Appl. Phys. Lett.* **2001,** *78*, 2285-2287.
(35) Cao, B.; Cai, W.; Zeng, H. Temperature-Dependent Shifts of Three Emission Bands for ZnO Nanoneedle Arrays. *Appl. Phys. Lett.* **2006,** *88*, 161101.
(36) Li, L. M.; Du, Z. F.; Wang, T. H. Enhanced Sensing Properties of Defect-Controlled ZnO Nanotetrapods Arising from Aluminum Doping. *Sens. Actuators B* **2010,** *147*, 165-169.
(37) Ahn, M.-W.; Park, K.-S.; Heo, J.-H.; Park, J.-G.; Kim, D.-W.; Choi, K. J.; Lee, J.-H.; Hong, S.-H. Gas Sensing Properties of Defect-Controlled ZnO-Nanowire Gas Sensor. *Appl. Phys. Lett.* **2008,** *93*, 263103.
(38) Dingle, R. Luminescent Transitions Associated with Divalent Copper Impurities and the Green Emission From Semiconducting Zinc Oxide. *Phys. Rev. Lett.* **1969,** *23*, 579.
(39) Morkoç, H.; Özgür, Ü., *Zinc Oxide: Fundamentals, Materials and Device Technology*. John Wiley & Sons: **2008**.
(40) Reynolds, D. C.; Look, D. C.; Jogai, B. Fine Structure on the Green Band in ZnO. *J. Appl. Phys.* **2001,** *89*, 6189-6191.
(41) Nobis, T.; Kaidashev, E. M.; Rahm, A.; Lorenz, M.; Grundmann, M. Whispering Gallery Modes in Nanosized Dielectric Resonators with Hexagonal Cross Section. *Phys. Rev. Lett.* **2004,** *93*, 103903.
(42) Cuscó, R.; Alarcón-Lladó, E.; Ibáñez, J.; Artús, L.; Jiménez, J.; Wang, B.; Callahan, M. J. Temperature Dependence of Raman Scattering in ZnO. *Phys. Rev. B* **2007,** *75*, 165202.
(43) Martin, R. M.; Damen, T. C. Breakdown of Selection Rules in Resonance Raman Scattering. *Phys. Rev. Lett.* **1971,** *26*, 86-88.
(44) Ye, J. D.; Tripathy, S.; Ren, F.-F.; Sun, X. W.; Lo, G. Q.; Teo, K. L. Raman-active Fröhlich optical phonon mode in arsenic implanted ZnO. *Appl. Phys. Lett.* **2009,** *94*, 011913.
(45) Wang, J. B.; Zhong, H. M.; Li, Z. F.; Lu, W. Raman study of N^+-implanted ZnO. *Appl. Phys. Lett.* **2006,** *88*, 101913.
(46) Meyer, B. K.; Alves, H.; Hofmann, D. M.; Kriegseis, W.; Forster, D.; Bertram, F.; Christen, J.; Hoffmann, A.; Straßburg, M.; Dworzak, M.; Haboeck, U.; Rodina, A. V. Bound Exciton and Donor–Acceptor Pair Recombinations in ZnO. *Phys. Status Solidi B* **2004,** *241*, 231-260.
(47) Heitz, R.; Hoffmann, A.; Broser, I. Fe^{3+} Center in ZnO. *Phys. Rev. B* **1992,** *45*, 8977-8988.
(48) Monteiro, T.; Boemare, C.; Soares, M. J.; Rita, E.; Alves, E. Photoluminescence and Damage Recovery Studies in Fe-Implanted ZnO Single Crystals. *J. Appl. Phys.* **2003,** *93*, 8995-9000.
(49) Chang, J. F.; Kuo, H. H.; Leu, I. C.; Hon, M. H. The Effects of Thickness and Operation Temperature on ZnO:Al Thin Film CO Gas Sensor. *Sens. Actuators B* **2002,** *84*, 258-264.
(50) Cretu, V.; Postica, V.; Mishra, A. K.; Hoppe, M.; Tiginyanu, I.; Mishra, Y. K.; Chow, L.; de Leeuw, N. H.; Adelung, R.; Lupan, O. Synthesis, Characterization and DFT Studies of

Zinc-doped Copper Oxide Nanocrystals for Gas Sensing Applications. *J. Mater. Chem. A* **2016,** *4*, 6527-6539.
(51) Chang, S. C. Oxygen chemisorption on tin oxide: Correlation between electrical conductivity and EPR measurements. *J. Vac. Sci. Technol.* **1980,** *17*, 366-369.
(52) Zhou, Q.; Chen, W.; Xu, L.; Peng, S. Hydrothermal Synthesis of Various Hierarchical ZnO Nanostructures and their Methane Sensing Properties. *Sensors* **2013,** *13*, 6171-6182.
(53) Lupan, O.; Chow, L.; Chai, G. A Single ZnO Tetrapod-Based Sensor. *Sens. Actuators B* **2009,** *141*, 511-517.
(54) Chai, G.; Lupan, O.; Chow, L.; Heinrich, H. Crossed Zinc Oxide Nanorods for Ultraviolet Radiation Detection. *Sens. Actuators A* **2009,** *150*, 184-187.
(55) Na, C. W.; Woo, H.-S.; Kim, I.-D.; Lee, J.-H. Selective Detection of NO_2 and C_2H_5OH Using a Co_3O_4-Decorated ZnO Nanowire Network Sensor. *Chem. Commun.* **2011,** *47*, 5148-5150.
(56) Lupan, O.; Chow, L.; Pauporté, T.; Ono, L. K.; Roldan Cuenya, B.; Chai, G. Highly Sensitive and Selective Hydrogen Single-Nanowire Nanosensor. *Sens. Actuators B* **2012,** *173*, 772-780.
(57) Lupan, O.; Cretu, V.; Postica, V.; Ahmadi, M.; Cuenya, B. R.; Chow, L.; Tiginyanu, I.; Viana, B.; Pauporté, T.; Adelung, R. Silver-Doped Zinc Oxide Single Nanowire Multifunctional Nanosensor with a Significant Enhancement in Response. *Sens. Actuators B* **2016,** *223*, 893-903.
(58) Zhou, H.; Qu, Y.; Zeid, T.; Duan, X. Towards Highly Efficient Photocatalysts Using Semiconductor Nanoarchitectures. *Energy Environ. Sci.* **2012,** *5*, 6732-6743.
(59) Datta, N.; Ramgir, N.; Kaur, M.; Kailasa Ganapathi, S.; Debnath, A. K.; Aswal, D. K.; Gupta, S. K. Selective H_2S Sensing Characteristics of Hydrothermally Grown ZnO-Nanowires Network Tailored by Ultrathin CuO Layers. *Sens. Actuators B* **2012,** *166–167*, 394-401.
(60) Zhang, Y.-B.; Yin, J.; Li, L.; Zhang, L.-X.; Bie, L.-J. Enhanced Ethanol Gas-Sensing Properties of Flower-like p-CuO/n-ZnO Heterojunction Nanorods. *Sens. Actuators B* **2014,** *202*, 500-507.
(61) Choi, S.-W.; Katoch, A.; Zhang, J.; Kim, S. S. Electrospun Nanofibers of CuO-SnO_2 Nanocomposite as Semiconductor Gas Sensors for H_2S Detection. *Sens. Actuators B* **2013,** *176*, 585-591.
(62) Katoch, A.; Abideen, Z. U.; Kim, H. W.; Kim, S. S. Grain-Size-Tuned Highly H_2-Selective Chemiresistive Sensors Based on ZnO–SnO_2 Composite Nanofibers. *ACS Appl. Mater. Interfaces* **2016,** *8*, 2486-2494.
(63) Mathur, S.; Veith, M.; Haas, M.; Shen, H.; Lecerf, N.; Huch, V.; Hüfner, S.; Haberkorn, R.; Beck, H. P.; Jilavi, M. Single-Source Sol-Gel Synthesis of Nanocrystalline $ZnAl_2O_4$: Structural and Optical Properties. *J. Am. Ceram. Soc.* **2001,** *84*, 1921-1928.
(64) Okal, J.; Zawadzki, M. Catalytic Combustion of Methane Over Ruthenium Supported on Zinc Aluminate Spinel. *Appl. Catal. A* **2013,** *453*, 349-357.
(65) Zhao, X.; Wang, L.; Xu, X.; Lei, X.; Xu, S.; Zhang, F. Fabrication and Photocatalytic Properties of Novel ZnO/$ZnAl_2O_4$ Nanocomposite with $ZnAl_2O_4$ Dispersed Inside ZnO Network. *AIChE* **2012,** *58*, 573-582.
(66) Karzel, H.; Potzel, W.; Köfferlein, M.; Schiessl, W.; Steiner, M.; Hiller, U.; Kalvius, G. M.; Mitchell, D. W.; Das, T. P.; Blaha, P. Lattice Dynamics and Hyperfine Interactions in ZnO and ZnSe at High External Pressures. *Phys. Rev. B* **1996,** *53*, 11425.
(67) Zhang, Y.; Guo, Z.; Gao, X.; Cao, D.; Dai, Y.; Zhao, H. First-Principles of Wurtzite ZnO (0001) and (0001) Surface Structures. *J. Semicond.* **2010,** *31*, 082001.
(68) Nyberg, M.; Nygren, M. A.; Pettersson, L. G. M.; Gay, D. H.; Rohl, A. L. Hydrogen Dissociation on Reconstructed ZnO Surfaces. *J. Phys. Chem.* **1996,** *100*, 9054-9063.

(69) Kornherr, A.; Nauer, G. E.; Sokol, A. A.; French, S. A.; Catlow, C. R. A.; Zifferer, G. Adsorption of Organosilanes at a Zn-Terminated ZnO (0001) Surface: Molecular Dynamics Study. *Langmuir* **2006,** *22*, 8036-8042.
(70) Mishra, A. K.; de Leeuw, N. H. Mechanistic Insights Into the Cu(I) Oxide-Catalyzed Conversion of CO_2 to Fuels and Chemicals: A DFT Approach. *J. CO_2 Utilization*.
(71) Xiangfeng, C.; Dongli, J.; Djurišic, A. B.; Leung, Y. H. Gas-Sensing Properties of Thick Film Based on ZnO Nano-Tetrapods. *Chem. Phys. Lett.* **2005,** *401*, 426-429.
(72) Delaunay, J.-J.; Kakoiyama, N.; Yamada, I. Fabrication of Three-Dimensional Network of ZnO Tetratpods and its Response to Ethanol. *Mater. Chem. Phys.* **2007,** *104*, 141-145.
(73) Van Hieu, N.; Duc Chien, N. Low-Temperature Growth and Ethanol-Sensing Characteristics of Quasi-One-Dimensional ZnO Nanostructures. *Phys. B* **2008,** *403*, 50-56.
(74) Calestani, D.; Zha, M.; Mosca, R.; Zappettini, A.; Carotta, M. C.; Di Natale, V.; Zanotti, L. Growth of ZnO Tetrapods for Nanostructure-Based Gas Sensors. *Sens. Actuators B* **2010,** *144*, 472-478.
(75) Zheng, K.; Gu, L.; Sun, D.; Mo, X.; Chen, G. The Properties of Ethanol Gas Sensor Based on Ti Doped ZnO Nanotetrapods. *Mater. Sci. Eng. B* **2010,** *166*, 104-107.
(76) Santhaveesuk, T.; Wongratanaphisan, D.; Choopun, S. Enhancement of Sensor Response by TiO_2 Mixing and Au Coating on ZnO Tetrapod Sensor. *Sens. Actuators B* **2010,** *147*, 502-507.

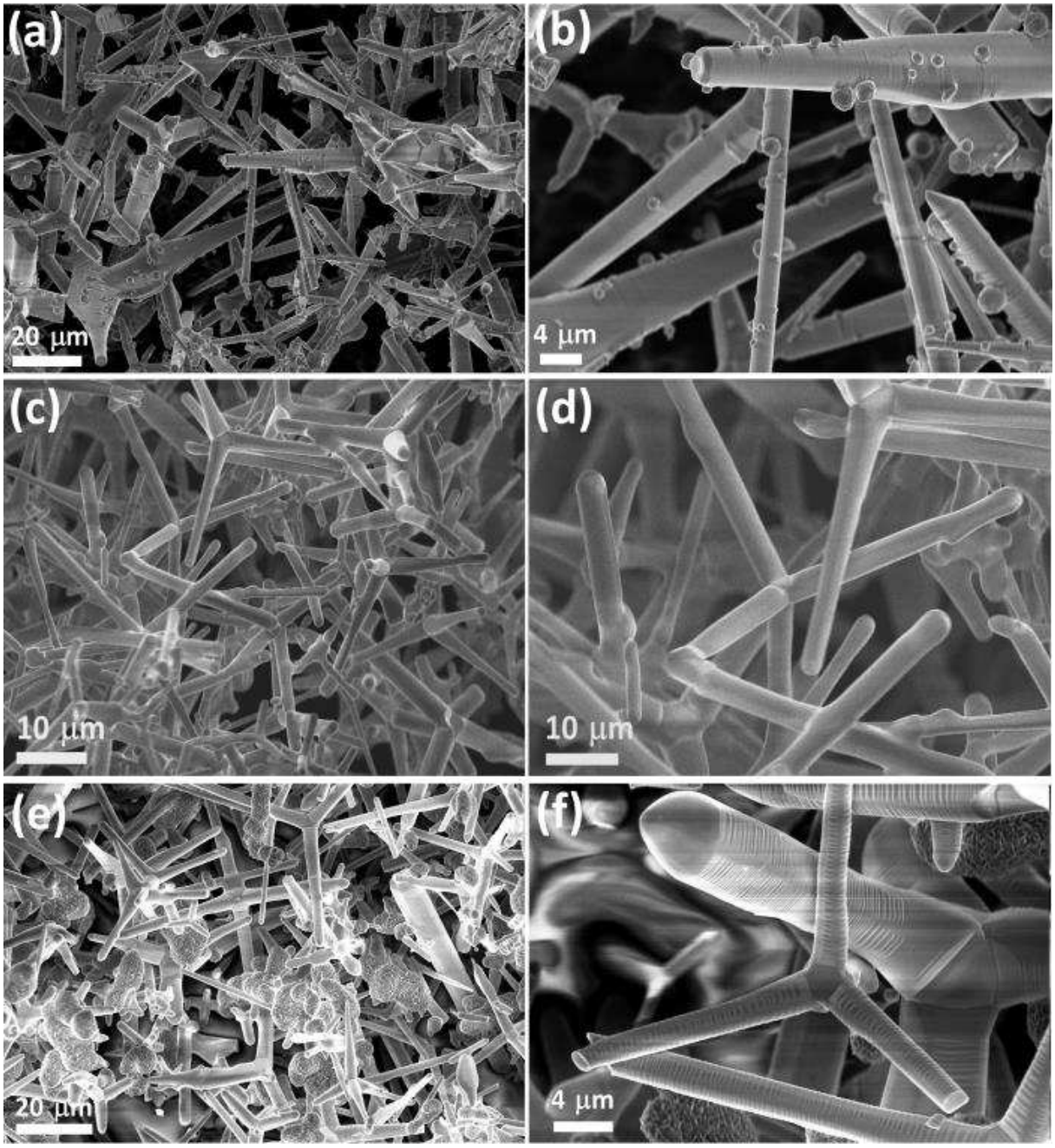

Figure 1. SEM images of synthesized hybrid network samples: (a,b) ZnO:Fe (weight ratio of 20:1); (c,d) ZnO:Cu (20:1); (e,f) ZnO:Al (10:1), at low and high magnifications, respectively.

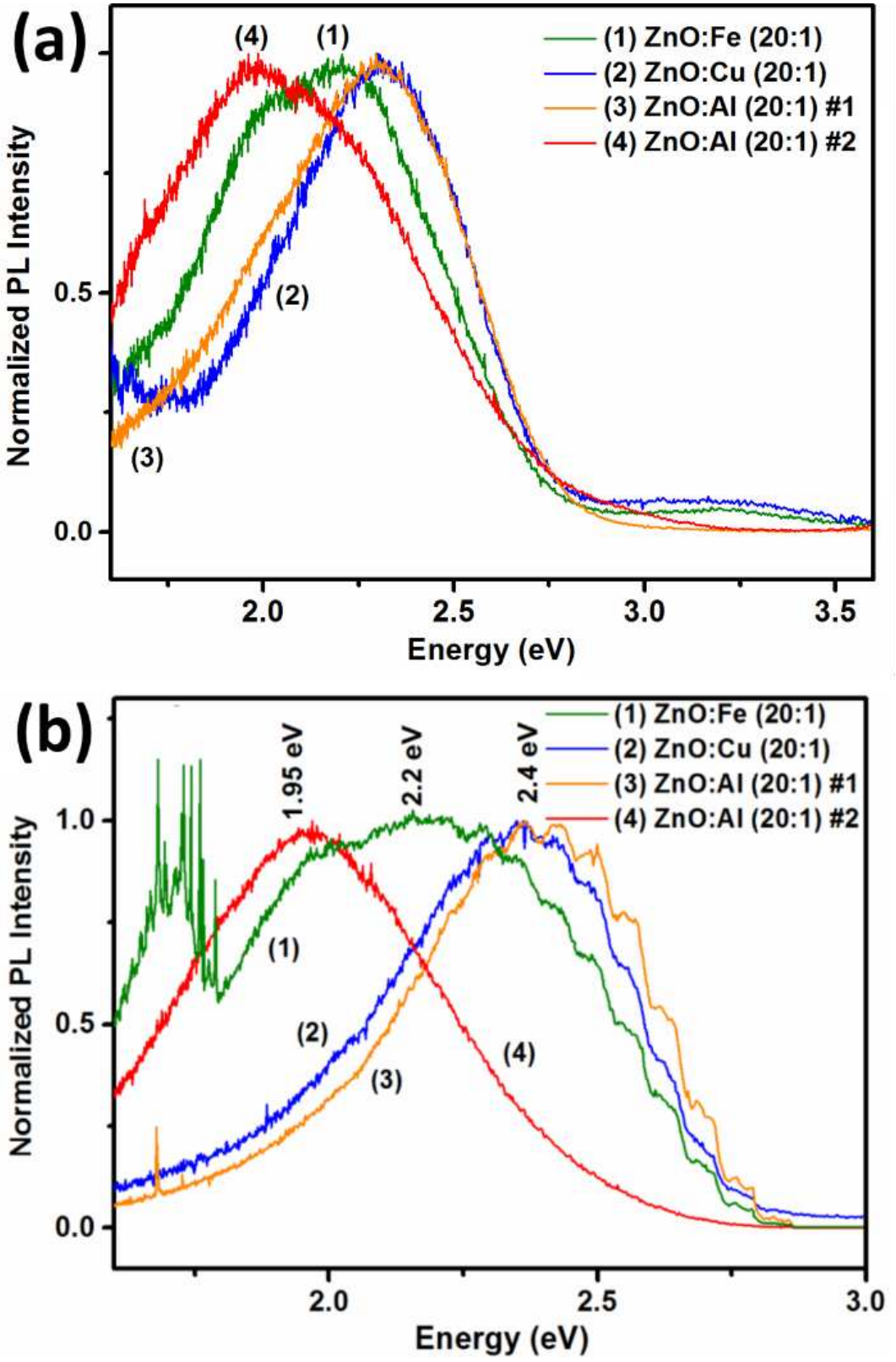

Figure 2. (a) Normalized RT PL of the studied samples, excited with 3.8 eV photon energy: (1) ZnO:Fe (weight ratio of 20:1); (2) ZnO:Cu (20:1) and (3,4) ZnO:Al (20:1) in different regions of the sample. (b) Normalized 10 K PL spectra of the same hybrid ZnO-T samples under the same excitation conditions.

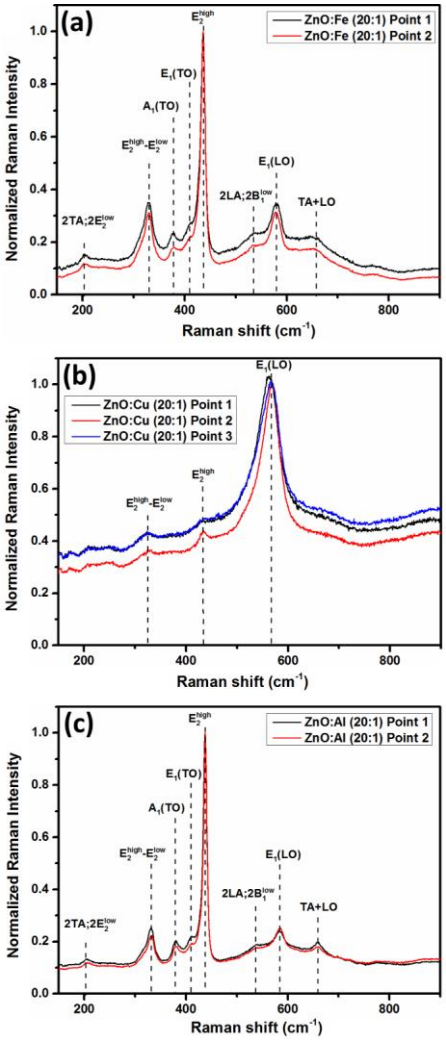

Figure 3. RT Raman results of: (a) ZnO:Fe (weight ratio of 20:1); (b) ZnO:Cu (20:1); (c) ZnO:Al (20:1), from 2-3 different points of the samples using a 442 nm line of a cw He-Cd laser.

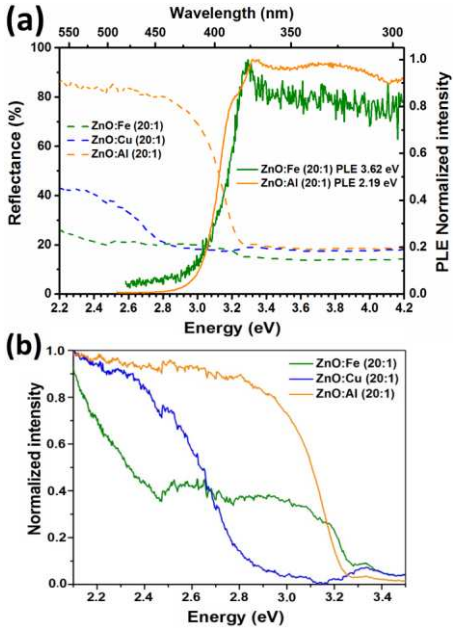

Figure 4. (a) RT diffuse reflectance (left *y*-axis, dashed lines) and RT PLE (right *y*-axis, full lines) results of the studied samples. (b) Normalized RT diffuse reflectance spectra of the networks.

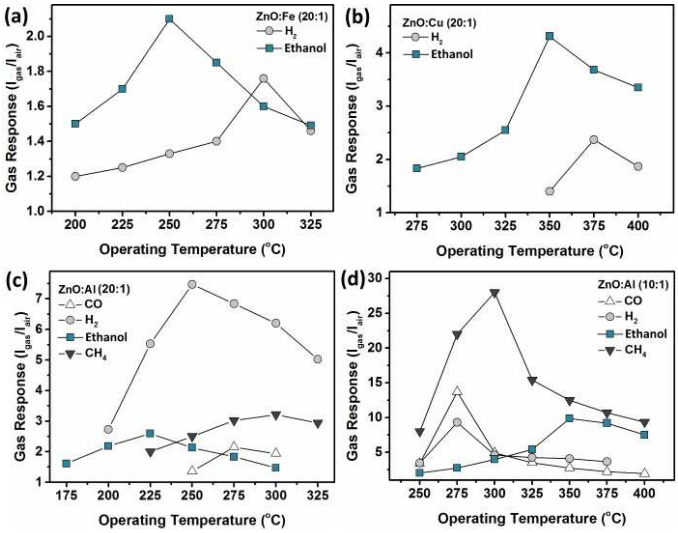

Figure 5. Gas response of devices towards CO, H_2, Ethanol vapour and CH_4 gases (100 ppm) at different operating temperatures for Me_xO_y and $Zn_xMe_{1-x}O_y$ doped and alloyed ZnO-T networks (Me = Fe, Cu or Al): (a) ZnO:Fe (20:1); (b) ZnO:Cu (20:1); (c) ZnO:Al (20:1); (d) ZnO:Al (10:1).

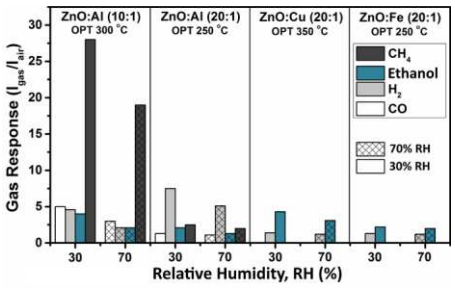

Figure 6. The gas response to CO, H_2, ethanol vapour and CH_4 of the Me_xO_y and $Zn_xMe_{1-x}O_y$ (Me=Fe,Cu,Al) doped and alloyed ZnO-T at their optimal operating temperature and different values of relative humidity (RH).

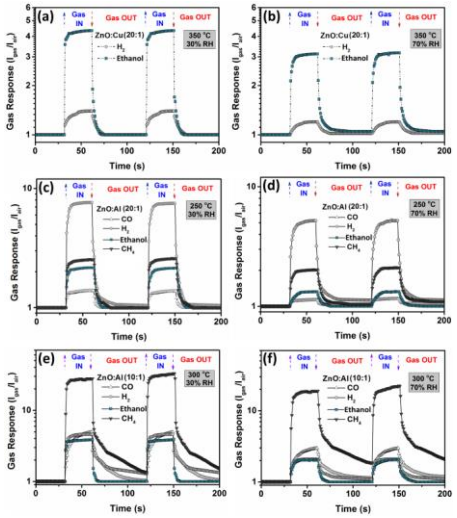

Figure 7. The transient gas response of the sensors based on Me_xO_y and $Zn_xMe_{1-x}O_y$ -alloyed ZnO-T hybrid networks at their optimal operating temperatures and at 30% (in left column) and 70% (in the right column) relative humidity (RH): (a,b) ZnO:Cu (20:1); (c,d) ZnO:Al (20:1); (e,f) ZnO:Al (10:1).

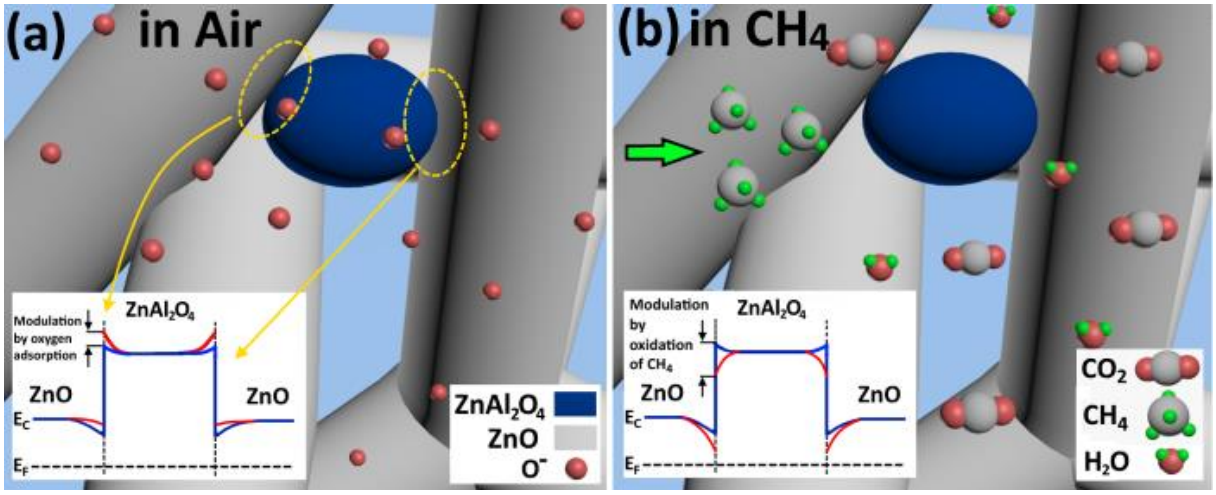

Figure 8. Schematic illustration of the gas sensing mechanism of the ZnO-T-$ZnAl_2O_4$ hybrid networks: (a) at exposure to air; and (b) at exposure to CH_4 gas. Modulation of the potential barriers between $ZnAl_2O_4$ and ZnO (evidenced by yellow circles) is performed by adsorption of the oxygen atoms (represented by red spheres). At exposure to CH_4 gas (or other oxidizing gases), due to released electrons, the height of potential barrier is decreasing.

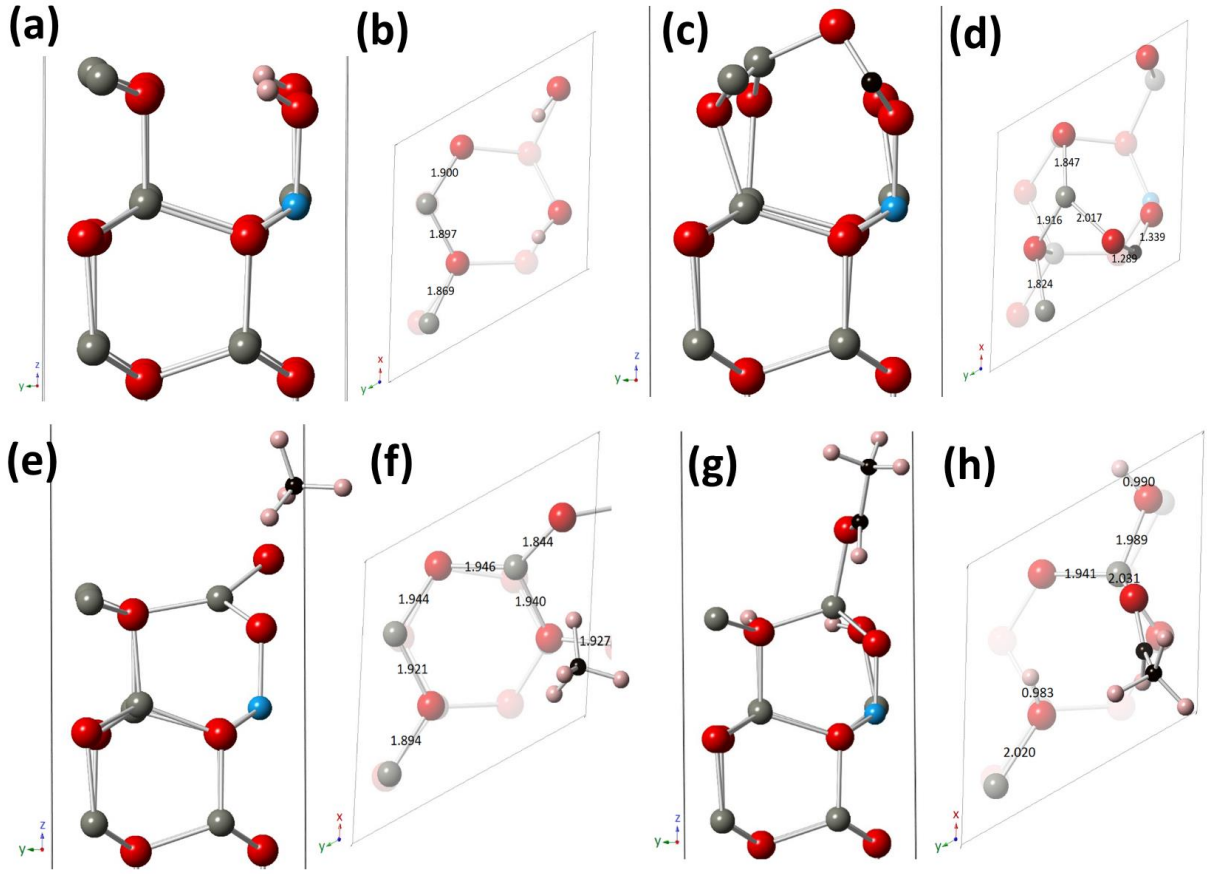

Figure 9. The optimized geometries of (a,b) H_2, (c,d) CO, (e,f) CH_4 and (g,h) CH_3CH_2OH molecules binding with the Al_2O_4:ZnO(0001) surface. Left and right panel show side and top views of surfaces. The Zn, O and Al atoms are represented by grey, red and light blue colours respectively, while C and H atoms are represented by black and salmon pink colours respectively.

Table 1. Parameters of sensors based on the ZnO-T networks

Dopant	**Gas (ppm)**	R_{gas}/R_{air}	**OPT (°C)**	τ_r	τ_d
Un-doped [71]	EtOH (1000) EtOH (100) CH_4 (1000)	130.7 29.4 ~42	300 300 270	20 s	20 s
Un-doped [72]	EtOH (50)	~25* ~4.2	400 300	n/a	> 100 s*
Un-doped [73]	EtOH (500) EtOH (100)	5.3 ~3.2*	300 300	25 s	25 s
Un-doped [74]	H_2S (1) NO_2 (20) EtOH (50) CO(10)	~25 ~20 ~20 <0.2	300	n/a	n/a
Un-doped [36] Al-doped [36]	EtOH (100) EtOH (100)	~20* ~40*	300 300	n/a	n/a
Un-doped [75] Ti-doped [75]	EtOH (100) EtOH (100)	2.8 11.5	260 260	1.5 m	3.1 m
Un-doped [76] Au/Ti-doped [76]	EtOH (50) EtOH (50) EtOH (50)	~3* 19* 24*	320 320 340	n/a	n/a
ZnO T networks [3]	H_2 (100)	1.62	400	80 ms	180 ms
ZnO-T-$ZnAl_2O_4$ hybrid networks (ZnO:Al (20:1)) (this work)	**H_2 (100)**	**~ 7.5**	**250**	**4.7 s**	**3.6 s**
ZnO-T-$ZnAl_2O_4$ hybrid networks (ZnO:Al (10:1)) (this work)	**CH_4 (100)**	**28**	**300**	**17.8 s**	**21 s**
ZnO-T-CuO hybrid networks (ZnO:Cu (20:1)) (this work)	**EtOH(100)**	**4.3**	**350**	**3.18 s**	**2.8 s**
ZnO-T-Fe_2O_3 hybrid networks (ZnO:Fe (20:1)) (this work)	**EtOH(100)**	**2.2**	**250**	**2.67 s**	**2.97 s**

The table of contents entry (ToC)

A novel method to improve and tune gas sensing properties of the ZnO tetrapod networks by alloying with Me_xO_y and $Zn_xMe_{1-x}O_y$ is reported. Due to the catalytic effect of the alloyed materials (Me=Fe, Cu or Al), a change in selectivity of the hybrid networks is demonstrated. Synthesized highly porous hybrid networks can serve as a novel material for developing highly selective gas sensors.

O. Lupan,[1,] V. Postica,[2] J. Gröttrup,[1] A. K. Mishra,[3] Nora H. de Leeuw,[3,4,*] J. F. C. Carreira,[5] J. Rodrigues,[5] N. Ben Sedrine,[5] M. R. Correia,[5,*] Teresa Monteiro,[5] V. Cretu,[2] I. Tiginyanu,[2] Daria Smazna,[1] Y. K. Mishra,[1] R. Adelung[1,*]*

Title

Hybridization of zinc oxide tetrapods for selective gas sensing applications

ToC figure